

NASA Technical Memorandum 4398

In-Flight Leading-Edge Extension  
Vortex Flow-Field Survey  
Measurements on a F-18 Aircraft  
at High Angle of Attack

David M. Richwine and David F. Fisher

SEPTEMBER 1992



NASA Technical Memorandum 4398

In-Flight Leading-Edge Extension  
Vortex Flow-Field Survey  
Measurements on a F-18 Aircraft  
at High Angle of Attack

David M. Richwine  
*PRC Inc.*  
*Edwards, California*

David F. Fisher  
*Dryden Flight Research Facility*  
*Edwards, California*



National Aeronautics and  
Space Administration

Office of Management

Scientific and Technical  
Information Program

1992

# CONTENTS

<b>TABLES</b>	iv
<b>FIGURES</b>	v
<b>ABSTRACT</b>	1
<b>NOMENCLATURE</b>	1
<b>INTRODUCTION</b>	2
<b>EXPERIMENT DESCRIPTION</b>	3
Vehicle Description . . . . .	3
LEX Survey Rake Description and Calibration . . . . .	3
Instrumentation and Data Reduction Technique . . . . .	4
<b>FLIGHT TEST CONDITIONS</b>	5
<b>RESULTS AND DISCUSSION</b>	5
Description of F-18 Leading-Edge Extension Flow Field . . . . .	5
Leading-Edge Extension Vortex Flow-Field Measurements . . . . .	6
Flow-Field Measurements, $\alpha \approx 19^\circ$ and $30^\circ$ . . . . .	6
Effect of Angle of Attack . . . . .	7
Comparison of Leading-Edge Extension Vortex Flow-Field Measurements . . . . .	8
Comparison with Flight Surface Pressure and Flow Visualization Results, $\alpha \approx 19^\circ$ and $30^\circ$ . . . . .	8
Comparison with Computational Solutions, $\alpha \approx 19^\circ$ and $30^\circ$ . . . . .	8
<b>CONCLUDING REMARKS</b>	10
<b>REFERENCES</b>	11
<b>TABLES</b>	13
<b>FIGURES</b>	14

## TABLES

1	The X-29A aircraft physical characteristics . . . . .	13
2	LEX survey rake flight test summary . . . . .	13

## FIGURES

1	NASA F-18 HARV . . . . .	14
2	LEX survey rake . . . . .	15
(a)	Hemispherical-tipped five-hole probe . . . . .	15
(b)	Five-hole probe nomenclature . . . . .	15
(c)	Survey rake . . . . .	15
3	LEX survey rake located on the upper surface of the right LEX with the probe tips located at F.S. 253 . . . . .	16
4	Typical calibration data sets . . . . .	17
(a)	Flow angularity . . . . .	17
(b)	Total pressure . . . . .	17
(c)	Static pressure . . . . .	17
5	Grid of measured data points . . . . .	18
6	History of F-18 HARV during flight test . . . . .	19
(a)	$\alpha = 19.4^\circ$ , $\beta = -0.2^\circ$ , $M = 0.28$ . . . . .	19
(b)	$\alpha = 30.0^\circ$ , $\beta = -0.3^\circ$ , $M = 0.24$ . . . . .	19
7	View from wingtip of LEX vortex core and core breakdown (ref. 20) . . . . .	20
(a)	$\alpha = 20.0^\circ$ , $\beta = 0.0^\circ$ . . . . .	20
(b)	$\alpha = 29.8^\circ$ , $\beta = 0.2^\circ$ . . . . .	20
(c)	$\alpha = 42.5^\circ$ , $\beta = 0.8^\circ$ . . . . .	20
8	F-18 LEX flow field . . . . .	21
(a)	Surface flow visualization on the F-18 HARV left LEX, $\alpha \approx 30^\circ$ , (ref. 22) . . . . .	21
(b)	Schematic of crossflow about LEX . . . . .	21
9	LEX vortex flow-field measurements; $\alpha \approx 19^\circ$ , $\beta \approx -0.2^\circ$ , $M \approx 0.28$ , $Re \approx 12.0 \times 10^6$ . . . . .	22
(a)	Static pressure coefficient contours . . . . .	22
(b)	Total pressure coefficient contours . . . . .	22
(c)	Normalized dynamic pressure contours . . . . .	23
(d)	Normalized axial velocity contours . . . . .	23
(e)	Normalized crossflow velocity vectors . . . . .	24
10	LEX vortex flow-field measurements; $\alpha \approx 30^\circ$ , $\beta \approx -0.3^\circ$ , $M \approx 0.24$ , $Re \approx 9.4 \times 10^6$ . . . . .	25
(a)	Static pressure coefficient contours . . . . .	25
(b)	Total pressure coefficient contours . . . . .	25
(c)	Normalized dynamic pressure contours . . . . .	26
(d)	Normalized axial velocity contours . . . . .	26
(e)	Normalized crossflow velocity vectors . . . . .	27
11	Effect of angle of attack on LEX . . . . .	28
(a)	Normalized dynamic pressure contours, $\alpha \approx 19^\circ$ . . . . .	28
(b)	Crossflow velocity vectors, $\alpha \approx 19^\circ$ . . . . .	28
(c)	Normalized dynamic pressure contours, $\alpha \approx 26^\circ$ . . . . .	29
(d)	Crossflow velocity vectors, $\alpha \approx 26^\circ$ . . . . .	29
(e)	Normalized dynamic pressure contours, $\alpha \approx 30^\circ$ . . . . .	30
(f)	Crossflow velocity vectors, $\alpha \approx 30^\circ$ . . . . .	30
(g)	Normalized dynamic pressure contours, $\alpha \approx 36^\circ$ . . . . .	31

(h)	Crossflow velocity vectors, $\alpha \approx 36^\circ$ . . . . .	31
(i)	Normalized dynamic pressure contours, $\alpha \approx 48^\circ$ . . . . .	32
(j)	Crossflow velocity vectors, $\alpha \approx 48^\circ$ . . . . .	32
12	Effect of angle of attack on LEX vortex core location . . . . .	33
13	Minimum static pressure coefficients in LEX vortex core as a function of angle of attack	34
14	Effect of angle of attack on nondimensionalized LEX vortex core diameter and vertical location . . . . .	34
15	Off-surface LEX vortex static pressure coefficient contours and comparison to surface static pressure coefficient distributions and on-surface flow visualization results . . . .	35
(a)	$\alpha \approx 19^\circ$ . . . . .	35
(b)	$\alpha \approx 30^\circ$ . . . . .	35
16	Lateral position of vortex core and maximum suction pressure peak location as a function of angle of attack . . . . .	36
17	LEX vortex flow-field measurements and comparison to computational solutions, $\alpha \approx 19^\circ$ . . . . .	37
(a)	Static pressure coefficient contours, flight data . . . . .	37
(b)	Static pressure coefficient contours, computational solution . . . . .	37
(c)	Dynamic pressure contours flight data . . . . .	38
(d)	Dynamic pressure contours, computational solution . . . . .	38
(e)	Crossflow velocity vectors, flight data . . . . .	39
(f)	Crossflow velocity vectors, computational solution . . . . .	39
18	LEX vortex flow-field measurements and comparison to computational solutions, $\alpha \approx 30^\circ$ . . . . .	40
(a)	Static pressure coefficient contours, flight data . . . . .	40
(b)	Static pressure coefficient contours, computational solution . . . . .	40
(c)	Dynamic pressure contours, flight data . . . . .	41
(d)	Dynamic pressure contours, computational solution . . . . .	41
(e)	Crossflow velocity vectors, flight data . . . . .	42
(f)	Crossflow velocity vectors, computational solution . . . . .	42

## ABSTRACT

Flow-field measurements on the leading-edge extension (LEX) of the F-18 High Alpha Research Vehicle (HARV) were obtained using a rotating rake with 16 hemispherical-tipped five-hole probes. Detailed pressure, velocity, and flow direction data were obtained through the LEX vortex core. Data were gathered during 1- $g$  quasi-stabilized flight conditions at angles of attack ( $\alpha$ ) from  $10^\circ$  to  $52^\circ$  and at Reynolds numbers based on mean aerodynamic chord up to  $16 \times 10^6$ . Normalized dynamic pressures and crossflow velocities clearly showed the primary vortex above the LEX and formation of a secondary vortex at higher angles of attack. The vortex was characterized by a ring of high dynamic pressure surrounding a region of low dynamic pressure at the vortex core center. The vortex core, subcore diameter, and vertical location of the core above the LEX increased with angle of attack. Minimum values for static pressure were obtained in the vortex subcore and decreased nearly linearly with increasing angle of attack until vortex breakdown. Rake-measured static pressures were consistent with previously documented surface pressures and showed good agreement with flow visualization flight test results. Comparison of the LEX vortex flight test data to computational solutions at  $\alpha \approx 19^\circ$  and  $30^\circ$  showed fair correlation.

## NOMENCLATURE

$C_p$	static pressure coefficient, $(p_s - p_\infty)/q_\infty$
$C_{pt}$	total pressure coefficient, $(p_t - p_\infty)/q_\infty$
F.S.	fuselage station, in.
$g$	load factor normal to longitudinal axis of aircraft
HARV	High Alpha Research Vehicle
LEX	leading-edge extension
LSR	LEX survey rake
$M$	free-stream Mach number
m.a.c.	mean aerodynamic chord, 11.525 ft for F-18 aircraft
$p_i$	pressure at probe port $i$ , lb/ft <sup>2</sup>
$p_s$	probe corrected static pressure, lb/ft <sup>2</sup>
$p_t$	probe corrected total pressure, lb/ft <sup>2</sup>
$p_\infty$	free-stream static pressure, lb/ft <sup>2</sup>
$p_{t\infty}$	free-stream total pressure, lb/ft <sup>2</sup>
$q$	probe corrected dynamic pressure, lb/ft <sup>2</sup>
$q_\infty$	free-stream dynamic pressure, lb/ft <sup>2</sup>
$R_1$	primary reattachment line location
$R_2$	secondary reattachment line location
$R_3$	tertiary reattachment line location
$Re$	Reynolds number based on m.a.c.
$S_1$	primary separation line location
$S_2$	secondary separation line location
$S_3$	tertiary separation line location
$s$	local span distance from LEX-fuselage junction to LEX leading edge at F.S. 253, 14.84 in.

$U_\infty$	free-stream velocity, ft/sec
$u, v, w$	axial, lateral, and vertical local velocity components as measured by each probe, respectively, ft/sec
$y$	distance along LEX local semispan starting inboard at the LEX-fuselage junction, in.
$z$	distance above LEX surface at $y/s = 0.87$ , in.
$\alpha$	aircraft angle of attack, from right wingtip angle-of-attack vane corrected for upwash, deg
$\beta$	aircraft angle of sideslip, average of left- and right-wingtip sideslip vanes corrected for angle of attack, deg
$\Delta p_\alpha$	difference in pressure between probe pitch ports, $p_6 - p_5$ , lb/ft <sup>2</sup>
$\Delta p_\beta$	difference in pressure between probe yaw ports, $p_3 - p_4$ , lb/ft <sup>2</sup>
$\Psi$	yaw angle measured by the probe, deg

## INTRODUCTION

To obtain high levels of aircraft performance and control at high angles of attack, many modern fighter designs include strakes or sharp, highly swept leading-edge extensions, which tend to promote vortical flows. These vortical flows can have a strong impact on aircraft performance from factors such as maximum lift, aircraft stability and control, and buffet. Therefore, it has become increasingly important to understand these vortical flows and to develop and validate reliable prediction methods with flight data. Vortex studies have been performed using subscale models in ground tests to obtain vortex flow-field measurements, usually at very low Reynolds numbers (refs. 1–8). However, only limited in-flight vortex flow-field measurements have been obtained on full-scale vehicles at flight Reynolds numbers.

The NASA High Alpha Technology Program was established to: increase the understanding of vortical flows, improve prediction techniques, provide design guidelines, and investigate new concepts for vortex control on advanced, highly maneuverable aircraft at high angles of attack ( $\alpha$ ). This program utilizes the F-18 configuration for validation and in-flight research. The program consists of wind-tunnel testing using subscale models (refs. 9, 10) and full-scale models and components, the development and refinement of computational fluid dynamics (CFD) solutions (refs. 11–15) and piloted simulations, and full-scale flight testing (refs. 16–25).

Part of this program includes research on the flow field about the F-18 High Alpha Research Vehicle (HARV). At high angles of attack, the F-18 flow field is dominated by vortical flows from the leading-edge extensions (LEXs) and forebody. Detailed pressure, velocity, and flow direction data were obtained at one station on the LEX to gain quantitative data in the F-18 LEX vortex flow field. These data complement the qualitative in-flight flow visualization data (refs. 16–21) and will be used to correlate with the surface pressure data (ref. 22) previously obtained.

This paper presents flow-field measurements of the LEX vortex obtained in flight using a rotating rake with 16 hemispherical-tipped five-hole probes. Data were gathered at 1- $g$  flight conditions at quasi-stabilized angles of attack from 10° to 52° and at Reynolds numbers based on mean aerodynamic chord



(m.a.c.) up to  $16 \times 10^6$ . Correlations with surface pressures, flow visualization, and computational fluid dynamics results are presented at  $\alpha \approx 19^\circ$  and  $30^\circ$ .

The authors would like to thank the following from NASA Dryden Flight Research Facility: the late Merle Economu and Greg Poteat for assistance in the conceptual development, design, and fabrication of the LEX survey rake, and John Jarvis and John Saltzman for their software development and data reduction efforts. The authors also would like to thank Daniel Banks, Frank Quinto, and Scott Kjelgaard of NASA Langley Research Center for their assistance in the wind-tunnel testing and calibration of the LEX survey rake. Thanks are also due to Dr. Yehia Rizk of NASA Ames Research Center and Dr. Jim Thomas of NASA Langley Research Center for their significant contributions of computational results, which enabled valuable comparisons between flight test data and these computational results.

## EXPERIMENT DESCRIPTION

### Vehicle Description

The NASA F-18 HARV (ref. 23, fig. 1), is a single-place preproduction F-18 aircraft built by the McDonnell Douglas (St. Louis, Missouri) and Northrop (Newbury Park, California) Corporations. It is powered by two General Electric (Lynn, Massachusetts) F404-GE-400 afterburning turbofan engines. The aircraft features a mid-wing with leading- and trailing-edge flaps that operate on a schedule that is a function of angle of attack and Mach number ( $M$ ). For  $M \leq 0.76$  and  $\alpha \geq 26^\circ$ , the leading-edge flap is down  $33^\circ$  (maximum), and the trailing-edge flap is at zero. The LEXs are mounted on each side of the fuselage from the wing roots to just forward of the windscreen. The aircraft has twin vertical stabilizers canted out  $20^\circ$  from the vertical and differential all-moving horizontal stabilators. The NASA F-18 HARV, with the current flight control computers and control laws, is flown by NASA pilots in the fighter escort configuration without stores. The aircraft carries no missiles and the wingtip Sidewinder launch racks have been replaced with special camera pods and wingtip airdata booms. The flight test noseboom was removed from the aircraft and a NASA flush airdata system was installed (ref. 24). The aircraft has an unrestricted angle-of-attack flight envelope in this configuration with the center of gravity between 17 and 25 percent of the m.a.c. of 11.525 ft.

### LEX Survey Rake Description and Calibration

The LEX survey rake (LSR) consisted of 16 0.125-in. outside diameter, hemispherical-tipped, five-hole probes mounted at 1-in. intervals into a thin  $20^\circ$  leading-edge angle blade as shown in figure 2. In addition to the five pressure ports at the tip to measure total pressure and flow angularity, a manifolded ring of four static pressure ports was located 1.00 in. aft of the tip. When mounted into the blade, the static pressure ports were 7.2 blade thicknesses forward of the blade maximum thickness. For a similar single probe in ideal free-stream conditions with a transverse strut presented in reference 26, data indicate that errors of  $\Delta p/q < 0.01$  can be expected at Mach numbers  $< 0.5$ . An electric motor rotated the LSR about a longitudinal axis on the LEX. The LSR rotated from a position adjacent to the canopy to a position near the upper surface of the LEX (approximately  $144^\circ$ ) and then back in approximately 22 sec. The rake rotation angle was measured by a potentiometer mounted on the shaft. As shown in figure 3, a fairing covered the motor, potentiometer, and supporting structure. The rake

was mounted on the right LEX with the probe tips located at aircraft fuselage station (F.S.) 253. This location coincides with a row of surface pressure orifices on the LEX. These data (ref. 22) will be used for correlation.

Calibration data for the LSR probes were obtained at NASA Langley Research Center's 14- by 22-Foot Subsonic Tunnel, which is a closed-circuit, single-return, atmospheric wind tunnel (ref. 27). Calibrations were obtained at a tunnel free-stream dynamic pressure of 90 lb/ft<sup>2</sup> with calibration checks made at 70 and 110 lb/ft<sup>2</sup>. Reynolds number effects on the probes were expected to be insignificant since the Reynolds number based on probe diameter, < 14,500, was much less than the critical Reynolds number for a sphere.

The probes were calibrated for flow angularity, total pressure, static pressure, and dynamic pressure in the pitch and yaw axes out to  $\pm 50^\circ$ . Typical calibrations for a probe are shown in figure 4. Figure 4(a) shows the sensitivity of the two diametrically opposed orifice pairs in the pitch and yaw axes. Smooth curves were drawn through the data points for each probe orifice pair and used as the calibration curve for the appropriate axes.

Using a similar procedure, calibrations were obtained for total pressure (fig. 4(b)) and static pressure (fig. 4(c)). These calibrations were used to correct the measured values to free-stream conditions for flow angles out to  $45^\circ$ . Flow angles exceeded  $45^\circ$  in some areas of the flow field such as the shear layer from the leading edge of the LEX and the vortex subcore. The vortex subcore was defined as the region inside the core where  $q/q_\infty < 1$ . In these cases, extrapolations of the calibrations were necessary; calibration data from reference 1 were used as a guide to approximate these calibrations.

## Instrumentation and Data Reduction Technique

Airdata measurements from the F-18 HARV were obtained using wingtip airdata booms specially designed for high-angle-of-attack flight test. Both wingtip booms were calibrated at angles of attack up to  $50^\circ$  (ref. 25). Real-time free-stream conditions from the airdata system were used to provide reference flight conditions during each test point.

Three 32-channel electronically scanning differential pressure transducers with a range of  $\pm 720$  lb/ft<sup>2</sup> were mounted in the LEX just aft of the rake to measure the 96 pressures from the rake. These transducers were plumbed to a 50-in<sup>3</sup> reference tank monitored by an absolute pressure transducer located in the aircraft nose. Line lengths from the probe tip to the transducer were kept to a minimum. The longest lengths were approximately 28 in. of 0.025-in. inside diameter tubing and approximately 17 in. of 0.062-in. inside diameter tubing.

Table 1 shows estimated uncertainties in the data for a typical probe for flow angles of  $20^\circ$  and  $40^\circ$ . From the data uncertainties at flow angles of  $40^\circ$ , the estimated uncertainties for total pressure coefficient ( $C_{pt}$ ) and static pressure coefficient ( $C_p$ ), were  $\pm 0.06$  and  $\pm 0.05$ , respectively. The estimated uncertainty for  $q/q_\infty$  was  $\pm 0.04$ . Errors in the calculation of the axial, lateral, and vertical local velocity components ( $u$ ,  $v$ , and  $w$ ) normalized to free-stream velocity ( $U_\infty$ ) were  $\pm 0.03$ . However, in the areas where flow angles exceed  $\pm 45^\circ$ , the estimated uncertainty of the data is expected to increase.

The data from the 16 LSR probes and the corresponding reference flight conditions were processed approximately every  $2^\circ$  during a rake traverse as shown by the grid of figure 5. Data, flow angles, and coordinates were then transformed into the aircraft coordinate system. The matrix of these parameters was transferred to a graphics workstation and merged with a surface grid of the aircraft at F.S. 253.

## FLIGHT TEST CONDITIONS

The LSR data were obtained primarily at quasi-stabilized 1- $g$  flight conditions with angle of sideslip ( $\beta$ )  $\approx 0^\circ$ . In-flight zeros for the LSR pressure transducers were taken before each test point and applied to the postflight data processing. Each maneuver required quasi-stabilized flight conditions. The priority was to maintain steady angle of attack and angle of sideslip and obtain the 22 sec of flight data (11 sec/survey) required to complete a pair of surveys. Surveys of the flow field were obtained in pairs. This was done to obtain multiple data sets and to identify any possible hysteresis effects resulting from the outboard and inboard rotation of the LSR during a particular maneuver. Table 2 shows a summary of the flight test maneuvers and conditions for data included in this report.

Figure 6 shows time histories of the flight conditions during typical maneuvers. At  $\alpha \approx 19^\circ$  (fig. 6(a)), angle of attack and angle of sideslip are maintained within  $\pm 1.0^\circ$  with slight variations in free-stream dynamic pressure ( $q_\infty$ ), and a very slight increase in free-stream static pressure ( $p_\infty$ ). This indicates an altitude loss of 120 ft during the test point. At  $\alpha \approx 30^\circ$  (fig. 6(b)), angle of attack and angle of sideslip are maintained within  $\pm 1.5^\circ$  with  $q_\infty$  and  $p_\infty$  rising slightly and an altitude loss of 700 ft during the test point. These test points were typical with perturbations in angle of attack and angle of sideslip, and altitude loss increasing as angle of attack increased.

## RESULTS AND DISCUSSION

### Description of F-18 Leading-Edge Extension Flow Field

At high angles of attack, the F-18 flow field is dominated by vortices that separate from the forebody surface and at the sharp leading edges of each LEX. The LEX vortex cores are wound tightly and extend downstream until vortex core breakdown occurs. At  $\alpha \approx 20^\circ$  (fig. 7(a)), breakdown occurs near the leading edge of the vertical tails. As the angle of attack increases to  $30^\circ$  (fig. 7(b)), the vortex core breakdown moves forward to ahead of the wing leading edge. As the angle of attack increases further, vortex core breakdown continues to move forward. At  $42.5^\circ$  (fig. 7(c)), the vortex core breakdown is shown occurring near the LEX apex. The LEX vortex core breakdown occurs at the LSR location, F.S. 253, at  $\alpha \approx 38^\circ$  and  $\beta \approx 0^\circ$ . Further details on the LEX vortex core and breakdown location can be found in reference 20.

Figure 8 shows the effect of the LEX vortex on the surface flow on the LEX. An emitted fluid technique (ref. 16) was used to visualize surface flow streamlines (fig. 8(a)). Where the flow streamlines merge, lines of separation are defined and, conversely, where the streamlines diverge, lines of reattachment are defined. Figure 8(b) is a schematic of the cross-sectional view of crossflow about the LEX at high angles of attack. Flow separates in a shear layer from the leading edge of the LEX at the primary separation line location ( $S_1$ ) and forms the primary vortex above the upper surface of the LEX due to the

low-pressure region. The primary vortex induces a much smaller and weaker counterrotating secondary vortex that separates at the secondary separation line location ( $S_2$ ) (ref. 22), which corresponds to the end of pressure recovery of an adverse pressure gradient. The secondary vortex induces an even smaller and weaker tertiary vortex that separates at the tertiary separation line location ( $S_3$ ). Typical secondary and tertiary reattachment locations,  $R_2$  and  $R_3$  respectively, are shown in figure 8(b).

## Leading-Edge Extension Vortex Flow-Field Measurements

### Flow-Field Measurements, $\alpha \approx 19^\circ$ and $30^\circ$

The obtrusive effect of the LSR on the LEX vortex flow field and vortex breakdown was considered in the flight test and analysis of the vortex flow-field measurements. With the LSR installed no qualitative results were available, such as flow visualization of the LEX vortex with an operational LSR. However, the pilots observed no effect on the aircraft handling qualities. It is believed that the LSR effect is minor because of the small-sized probes and the thin blade of the rake, relative to the size and strength of the LEX vortex.

Flow-field measurements of the LEX vortex at F.S. 253 and at  $\alpha \approx 19^\circ$  and  $30^\circ$  are presented in figures 9 and 10. Each of these figures include contour plots of the LEX vortex flow field showing  $C_p$ ,  $C_{pt}$ ,  $q/q_\infty$ ,  $u/U_\infty$ , and a vector plot showing the resultant of the  $v/U_\infty$  and  $w/U_\infty$  crossflow velocities. For increased precision, the measured values of the data from the vortex core were extracted from the actual data rather than from the contour plots.

In figures 9(a) and (b), the low-pressure region of the vortex core can be observed in the static and total pressure coefficients at  $\alpha \approx 19^\circ$ . The minimum pressure coefficient measured for both  $C_p$  and  $C_{pt}$  was approximately  $-2.7$ . Normalized dynamic pressure was computed and figure 9(c) shows a ring of high dynamic pressure flow about a subcore of low dynamic pressure. Figure 9(d) shows a low axial velocity in the subcore and also a region of high axial velocity inboard of the subcore. Crossflow velocity vectors for  $\alpha \approx 19^\circ$  are presented in figure 9(e). This figure clearly shows the shear layer and rotation of the vortical flow about the core. The longer arrow lengths indicate the regions of high crossflow velocities.

Similar results for  $\alpha \approx 30^\circ$  are presented in figure 10. In figures 10(a) and (b) the minimum values were  $C_p \approx -4.2$  and  $C_{pt} \approx -3.2$ . As observed in figure 10(c), the vortex core and subcore have increased in size as compared to the same results at  $\alpha \approx 19^\circ$ . The ring of high dynamic pressure flow about a subcore of low dynamic pressure is observed again. As seen in figure 10(d), the region of high axial velocity inboard of the subcore has become more pronounced compared to the  $\alpha \approx 19^\circ$  data shown in figure 9(d). This unexpected region of high axial velocity could be the result of interactions caused by the proximity of the aircraft fuselage and canopy compared to the relatively small span of the LEX at F.S. 253. Indications of the secondary vortex formation are shown in the crossflow velocity vectors (fig. 10(e)). Identification of the secondary vortex from LSR data was limited at this angle of attack. This was because of the proximity of the secondary vortex to the LEX surface, which was beyond the survey limits of the LSR.

## Effect of Angle of Attack

Figure 11 presents the effect of angle of attack on the LEX vortex at F.S. 253 for  $\alpha = 19^\circ$  to  $48^\circ$ . Normalized dynamic pressure contour plots and velocity vector plots at  $\alpha \approx 19^\circ$ ,  $26^\circ$ ,  $30^\circ$ ,  $36^\circ$ , and  $48^\circ$  were selected to show the formation and progression of the LEX vortex flow through the range of high angles of attack achieved.

The normalized dynamic pressure contour plots and velocity vector plots show the primary vortex core and the shear layer separation from the LEX leading edge through the angle-of-attack range presented. Crossflow velocity vectors are consistent with the dynamic pressure contours and show the direction of rotation of the shear layer and the primary vortex core. Indications of the formation of a secondary vortex begin to occur at  $\alpha \approx 26^\circ$  (fig. 11(d)), with formation of the secondary vortex most visible at  $\alpha \approx 36^\circ$  (fig. 11(h)). The region of high axial velocity inboard of the subcore increases in both size and magnitude with increased angle of attack.

By  $\alpha \approx 48^\circ$ , the breakdown of the LEX vortex has moved to the LEX apex forward of F.S. 253. As shown in figures 11(i) and (j), the flow field has become more irregular and dispersed with no discernible primary vortex core as expected. The crossflow velocity vectors are surprisingly uniform and indicate that a relatively organized rotational flow field continues to exist despite core breakdown.

In figure 11, the contour and vector plots show that the LEX primary vortex core can be accurately identified, tracked, and quantified as a function of angle of attack. The coordinates of the vortex core center were identified and located using crossflow velocity vector plots. Core center locations were validated with the data from the contour plots at each appropriate angle of attack. The effect of angle of attack on the LEX vortex core location, pressures, and diameter for  $\alpha \approx 10^\circ$  to  $36^\circ$  are shown in figures 12–14. As shown in figure 12, the vertical location of the vortex core above the LEX surface increased with angle of attack, with only limited movement laterally. In figure 13, the minimum values for static pressure coefficient obtained in the vortex subcore are shown decreasing nearly linearly with increased angle of attack until vortex core breakdown. Beyond vortex core breakdown, the minimum values for static pressure coefficient in the region of vortical flow appear to rise. More data are needed to confirm this trend after vortex core breakdown.

In figure 14, the vortex core diameter, vortex subcore diameter, and the vertical location of the vortex core center were nondimensionalized with respect to the LEX span at F.S. 253 and plotted as a function of angle of attack. The core diameter was defined by the ring of maximum dynamic pressure about the subcore. The subcore diameter was defined as the boundary of the region inside the core where  $q/q_\infty \leq 1$ . The bars on the diameter measurements indicate the uncertainty of the measurement and the elliptical shape of the core and subcore. In addition to the increase in vertical location of the vortex core above the LEX surface, increases in the core and subcore diameters are observed with increased angle of attack up to vortex core breakdown.

## Comparison of Leading-Edge Extension Vortex Flow-Field Measurements

### Comparison with Flight Surface Pressure and Flow Visualization Results, $\alpha \approx 19^\circ$ and $30^\circ$

In figure 15, flight surface pressure and flow visualization results obtained previously on the HARV (ref. 22) were merged with the flow-field measurements of the LEX vortex obtained by the LSR at F.S. 253. On-surface static pressure distributions at F.S. 253 were included in the LSR data grid to provide an additional slice of data. This slice of data was used to fill the gap between the LSR data grid and the upper surface of the LEX with continuous contours of static pressure coefficients. Separation lines marked as  $S_1$ ,  $S_2$ , and  $S_3$  were obtained from surface flow visualization results similar to those previously shown in figure 8.

The smooth static pressure coefficient contours shown at  $\alpha \approx 19^\circ$  (fig. 15(a)) and  $\alpha \approx 30^\circ$  (fig. 15(b)) indicate good correlation between the surface and off-surface static pressures. Data in reference 22 show that as the vortical flow moved outboard on the LEX, the secondary separation line,  $S_2$ , occurred at the end of an adverse pressure gradient with a separated, flat pressure region outboard. The development of the secondary vortex is noted by the low-pressure region initiating from the secondary separation line shown in figure 15.

Previously reported results (refs. 5, 7, 8) indicate that for flat delta wings, the lateral location of the vortex core agreed well with the location of the maximum surface suction pressure peak. In addition, fair agreement was shown on the F-18 HARV (ref. 22), at locations on the LEX farther aft. As noted earlier in figure 12, angle of attack had little effect on the lateral position of the vortex core. Concurrently, as shown in figure 16, the lateral location of the maximum suction peak moves inboard as angle of attack is increased with limited correlation to the lateral location of the vortex core. This lack of agreement with previous studies (refs. 5, 7, 8) could be caused by the upper surface curvature of the LEX. In addition, this lack of agreement may also result from the size and proximity of the aircraft fuselage and canopy compared to the relatively small span of the LEX. In general, the vortex core center appeared to be located along the axis of a line normal to the LEX surface at the point where the maximum suction pressure peak occurred.

### Comparison with Computational Solutions, $\alpha \approx 19^\circ$ and $30^\circ$

Computational solutions of the F-18 LEX flow field at  $\alpha \approx 19^\circ$  (ref. 12), and more recently at  $30^\circ$  (ref. 14), were obtained from NASA Langley Research Center and NASA Ames Research Center, respectively, for comparison to flight test data. The computational solution at  $\alpha \approx 19^\circ$  used a surface definition for the F-18 forebody-LEX-only geometry and a flow field represented by approximately 370,000 points. Free-stream conditions used were  $M = 0.335$ ,  $\alpha = 19^\circ$ ,  $\beta = 0^\circ$ , with Reynolds number based on m.a.c. ( $Re$ ) =  $13.5 \times 10^6$ . The computational solution at  $\alpha \approx 30^\circ$  used a surface definition for a more complete F-18 aircraft that includes the forebody, LEX, faired-over inlet, wing, and deflected leading-edge flaps. Free-stream conditions used were  $M = 0.243$ ,  $\alpha = 30.3^\circ$ ,  $\beta = 0.0^\circ$ , with  $Re = 11.0 \times 10^6$ . Both of these computational solutions have been updated and refined to represent even more complete surface definitions of the F-18 aircraft than the solutions used for comparison in this paper.

Flow-field measurements of the LEX vortex and comparison to the computational solutions at  $\alpha \approx 19^\circ$  and  $30^\circ$  are presented in figures 17 and 18. Each figure includes flight test data and a

computational solution of the LEX vortex flow field for static pressure coefficient contours, dynamic pressure contours, and a vector plot showing the resultant of the crossflow velocities. Crossflow velocity vectors are expressed and normalized in terms of Mach number.

In figure 17, the comparison of flight test and computational results is shown for  $\alpha \approx 19^\circ$ . For flight test (figs. 17(a) and (b)), the minimum measured value of  $C_p$  in the primary vortex core is approximately  $-2.7$  compared to a computational  $C_p \approx -1.8$ . The overall shape of the  $C_p$  contours are similar, but the computational results appear to consistently underpredict the magnitude of  $C_p$  values. Both flight and CFD results (figs. 17(c) and (d)) indicate that the vortex core is characterized by the ring of high dynamic pressure about the subcore of low dynamic pressure. This ring is much stronger and better defined by flight data and shows a region of high dynamic pressure just inboard of the primary vortex core. Computational dynamic pressures show the region of highest dynamic pressure between the vortex core and LEX surface. Flight test results indicate that dynamic pressure at the vortex core center approaches zero while computational results predict a drop in dynamic pressure to a level near free-stream dynamic pressure.

The correlation between flight test and computational crossflow velocity vectors for  $\alpha \approx 19^\circ$  is shown in figures 17(e) and (f). Both results display vectors that are consistent and clearly show the direction of rotation of the shear layer and the primary vortex core. Computational results matched the vortex core center location obtained from flight test. However, the computational results tended to underpredict the magnitude of the crossflow velocities near the vortex core as indicated by the magnitude of the arrows in figures 17(e) and (f).

Figure 18 shows the comparison of flight test and computational results for  $\alpha \approx 30^\circ$ . The minimum measured value of  $C_p$  in the primary vortex core shows excellent agreement (figs. 18(a) and (b)), and is approximately  $-4.2$  for both flight test and computational results. The overall shape of the  $C_p$  contours are similar and even show the presence of the secondary vortex just above and inboard of the LEX leading edge. In addition, both results indicate that the vortex core is characterized by the ring of high dynamic pressure about a subcore of low dynamic pressure (figs. 18(c) and (d)). This ring continues to be better defined by flight data and shows a region of high dynamic pressure just inboard of the primary vortex core. Computational dynamic pressures (fig. 18(d)) continue to show the region of highest dynamic pressure between the vortex core and LEX surface. Flight test results continue to indicate that dynamic pressure in the vortex core center approaches zero while computational results predict a drop in dynamic pressure to a level near free-stream dynamic pressure.

The correlation between flight test and computational crossflow velocity vectors for  $\alpha \approx 30^\circ$  is shown in figures 18(e) and (f). Both results display vectors that are consistent and clearly show the direction of rotation of the shear layer, primary vortex core, and secondary vortex core. Computational results do not match the vortex core center location obtained from flight data. The computational results indicate a vortex core center location  $\Delta y/s = 0.13$  inboard from the vortex core center obtained from flight data. Again, the computational crossflow velocities tended to underpredict the magnitude of the crossflow velocities near the vortex core as indicated by the magnitude of the arrows in figures 18(e) and (f).

For overall comparison between flight test and computational results, various criteria were considered during correlation of these results. These criteria included the primary vortex core center location,

the magnitude of the pressure coefficients at this location, and the indication and location of a secondary vortex core at the appropriate angle of attack. Additional criteria include the general agreement between pressure contours and crossflow velocity vectors indicating similar flow patterns about the primary vortex core. These criteria were developed with the understanding that flight data would maintain local irregularities in the flow field while computational results would tend to have very smooth contours resulting from computational grid generation.

Using the previously mentioned criteria, fair correlation between flight test and computational results were obtained for  $\alpha \approx 19^\circ$  and  $30^\circ$ , considering the complexity of the flow field around the F-18 aircraft at high angles of attack. Flight test data at both angles of attack indicate that the primary vortex core consists of a ring of high dynamic pressure about the subcore of low dynamic pressure. This condition results in a low axial velocity at the core center. Several differences were identified between the flight data and computational results. Compared to the flight data, computational results show a minor drop in dynamic pressure resulting in a high axial velocity at the core center. The region of high dynamic pressure just inboard of the primary vortex core was not identified in the computational solutions. Both computational solutions tended to underpredict the magnitude of the crossflow velocities near the vortex core. In addition, the underprediction of pressure coefficient values with the  $\alpha \approx 19^\circ$  solution and slightly errant core location with the  $\alpha \approx 30^\circ$  solution are other areas that require further investigation. Some of these discrepancies may be caused by probe error in the vortex subcore and shear layer where flow angles exceeded  $45^\circ$ . Additional possible causes include the effects of rake installation on the LEX vortex and computational grid generation.

## CONCLUDING REMARKS

Flow-field measurements on the leading-edge extension (LEX) of the F-18 High Alpha Research Vehicle (HARV) have been obtained using a rotating rake with 16 hemispherical-tipped five-hole probes. Detailed pressure, velocity, and flow direction data were obtained through the LEX vortex core during 1-g quasi-stabilized flight conditions. The data were acquired at angles of attack ( $\alpha$ ) from  $10^\circ$  to  $52^\circ$  and at Reynolds numbers up to  $16 \times 10^6$  based on mean aerodynamic chord.

Normalized dynamic pressures and crossflow velocities clearly showed the primary vortex above the LEX and the formation of a secondary vortex at the higher angles of attack. The vortex was characterized by a ring of high dynamic pressure surrounding a region of low dynamic pressure at the vortex core center. The vortex core, subcore diameter, and vertical location of the core above the LEX increased with angle of attack.

Minimum values for static and total pressure were obtained in the vortex subcore with the minimum value for static pressure decreasing nearly linearly with increasing angle of attack until vortex breakdown. Static pressures measured by the rake were consistent and showed good agreement with previously documented surface pressures and flow visualization flight test results.

Comparison of the LEX vortex flight test data to computational solutions at  $\alpha \approx 19^\circ$  and  $30^\circ$  showed fair correlation considering the complexity of the flow field around the F-18 aircraft at high angles of attack. Several differences were identified between the flight data and computational results.



## REFERENCES

1. Kjelgaard, Scott O., *Theoretical Derivation and Calibration Technique of a Hemispherical-Tipped, Five-Hole Probe*, NASA TM-4047, 1988.
2. Kjelgaard, Scott O., and Sellers, William L., III, *Detailed Flow-Field Measurements Over a 75° Swept Delta Wing*, NASA TP-2997, 1990.
3. Verhaagen, N., and van Ransbeeck, P., "Experimental and Numerical Investigation of the Flow in the Core of a Leading Edge Vortex," AIAA-90-0384, Jan. 1990.
4. Payne, F.M., Ng, T.T., and Nelson, R.C., "Seven hole probe measurement of leading edge vortex flows," *Experiments in Fluids*, 7 (1989) pp. 1-8.
5. Hummel, D., "On the Vortex Formation Over a Slender Wing at Large Angles of Incidence," *High Angle of Attack Aerodynamics*, AGARD-CP-247, paper no. 15, 1979.
6. Bannink, W.J., and Nebbeling, C., "Measurements of the Supersonic Flow Field Past a Slender Cone at High Angles of Attack," *High Angle of Attack Aerodynamics*, AGARD-CP-247, paper no. 22, 1979.
7. Hummel, D., and Redeker, G., *Experimental Determination of Bound Vortex Lines and Flow in the Vicinity of the Trailing Edge of a Slender Delta Wing*, NASA Technical Translation, NASA TT-F-15,012, 1973.
8. Arena, Andrew S., Jr., and Nelson, Robert C., "Unsteady Surface Pressure Measurements on a Slender Delta Wing Undergoing Limit Cycle Wing Rock," AIAA-91-0434, Jan. 1991.
9. Banks, Daniel W., "Wind-Tunnel Investigation of the Forebody Aerodynamics of a Vortex-Lift Fighter Configuration at High Angles of Attack," SAE Technical Paper Series 881419, Oct. 1988.
10. Erickson, G.E., Hall, R.M., Banks, D.W., Del Frate, J.H., Schreiner, J.A., Hanley, R.J., and Pulley, C.T., "Experimental Investigation of the F/A-18 Vortex Flow at Subsonic Through Transonic Speeds, Invited Paper," AIAA-89-2222, July-Aug. 1989.
11. Thomas, James L., Walters, Robert W., Reu, Taekyu, Ghaffari, Farhad, Weston, Robert P., and Luckring, James M., "A Patched-Grid Algorithm for Complex Configurations Directed Towards the F/A-18 Aircraft," AIAA-89-0121, Jan. 1989.
12. Ghaffari, F., Luckring, J.M., Thomas, J.L., and Bates, B.L., "Navier-Stokes Solutions about the F/A-18 Forebody-LEX Configuration," AIAA-89-0338, Jan. 1989. Also published in *J. of Aircraft*, vol. 27, no. 9, pp. 737-748.
13. Cummings, Russell M., Rizk, Yehia M., Schiff, Lewis B., and Chaderjian, Neal M., "Navier-Stokes Predictions of the Flowfield Around the F-18 (HARV) Wing and Fuselage at Large Incidence," AIAA-90-0099, Jan. 1990.
14. Rizk, Yehia M., Schiff, Lewis B., and Gee, Ken, "Numerical Simulation Of The Viscous Flow Around A Simplified F/A-18 At High Angles of Attack," AIAA-90-2999, Aug. 1990.

15. Rizk, Yehia M., and Gee, Ken, "Numerical Prediction Of The Unsteady Flowfield Around The F-18 Aircraft At Large Incidence," AIAA-91-0020, Jan. 1991.
16. Fisher, David F., Richwine, David M., and Banks, Daniel W., *Surface Flow Visualization of Separated Flows on the Forebody of an F-18 Aircraft and Wind-Tunnel Model*, NASA TM-100436, 1988. Also published as AIAA-88-2112.
17. Curry, Robert E., and Richwine, David M., "An Airborne System for Vortex Flow Visualization on the F-18 High-Alpha Research Vehicle," AIAA-88-4671-CP, Sept. 1988.
18. Fisher, David F., and Meyer, Robert R., Jr., *Flow Visualization Techniques for Flight Research*, NASA TM-100455, 1988. Also published in *Flight Test Techniques*, AGARD-CP-452, paper no. 20.
19. Fisher, David F., Del Frate, John H., and Richwine, David M., "In-Flight Flow Visualization Characteristics of the NASA F-18 High Alpha Research Vehicle at High Angles of Attack," SAE 892222, Sept. 1989.
20. Del Frate, John H., and Zuniga, Fanny A., "In-Flight Flow Field Analysis on the NASA F-18 High Alpha Research Vehicle With Comparisons to Ground Facility Data," AIAA-90-0231, Jan. 1990.
21. Fisher, David F., Del Frate, John H., and Richwine, David M., *In-Flight Flow Visualization Characteristics of the NASA F-18 High Alpha Research Vehicle at High Angles of Attack*, NASA TM-4193, 1990.
22. Fisher, David F., Banks, Daniel W., and Richwine, David M., *F-18 High Alpha Research Vehicle Surface Pressures: Initial In-Flight Results and Correlation With Flow Visualization and Wind-Tunnel Data*, NASA TM-101724, 1990. Also published as AIAA-90-3018.
23. Schneider, Edward T., and Meyer, Robert R., Jr., "F-18 High Alpha Research Vehicle: Description, Results and Plans," SETP 33rd Symposium Proceedings, Sept. 1989.
24. Whitmore, Stephen A., Moes, Timothy R., and Larson, Terry J., *Preliminary Results From a Subsonic High Angle-of-Attack Flush Airdata Sensing (HI-FADS) System: Design, Calibration, and Flight Test Evaluation*, NASA TM-101713, 1990.
25. Moes, Timothy R., and Whitmore, Stephen A., *A Preliminary Look at Techniques Used to Obtain Airdata From Flight at High Angles of Attack*, NASA TM-101729, 1990.
26. Gracey, William, *Measurement of Aircraft Speed and Altitude*, NASA RP-1046, 1980, pp. 65.
27. Gentry, Garl L., Jr., Quinto, P. Frank, Gatlin, Gregory M., and Applin, Zachary T., *The Langley 14- by 22-Foot Subsonic Tunnel: Description, Flow Characteristics, and Guide for Users*, NASA TP-3008, 1990.

## TABLES

Table 1. Estimated uncertainties in the data for a typical probe.

Flow angle, deg	$p$ , lb/ft <sup>2</sup>	$\Psi$ , deg	$p_t$ , lb/ft <sup>2</sup>	$p_s$ , lb/ft <sup>2</sup>
20	$\pm 1.9$	$\pm 1.6$	$\pm 2.3$	$\pm 1.9$
40	$\pm 1.9$	$\pm 3.5$	$\pm 2.6$	$\pm 2.2$

Table 2. LEX survey rake flight test summary.

Point	$\alpha$ , deg	$\beta$ , deg	Mach	$Re$ ( $10^6$ )
1	$9.7 \pm 0.5$	$-0.1 \pm 0.5$	0.39	16.0
2	$15.4 \pm 0.5$	$-0.2 \pm 0.5$	0.31	13.0
3	$19.4 \pm 1.0$	$-0.2 \pm 1.0$	0.28	12.0
4	$23.0 \pm 1.0$	$-0.4 \pm 1.0$	0.29	12.0
5	$25.5 \pm 1.0$	$-0.5 \pm 1.0$	0.28	11.0
6	$28.1 \pm 1.5$	$0.0 \pm 1.0$	0.22	9.6
7	$30.0 \pm 1.5$	$-0.3 \pm 1.5$	0.24	9.4
8	$34.2 \pm 2.0$	$1.0 \pm 2.0$	0.23	8.5
9	$35.9 \pm 1.5$	$-0.3 \pm 3.0$	0.27	8.5
10	$47.8 \pm 1.5$	$0.3 \pm 5.0$	0.24	6.9
11	$52.1 \pm 1.5$	$2.2 \pm 3.5$	0.25	6.8

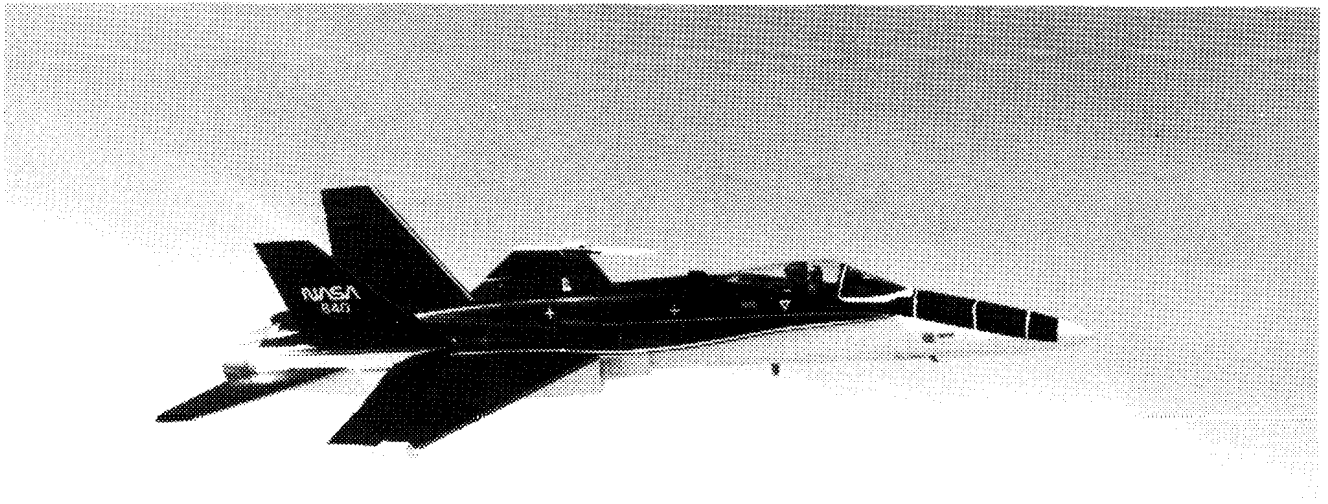
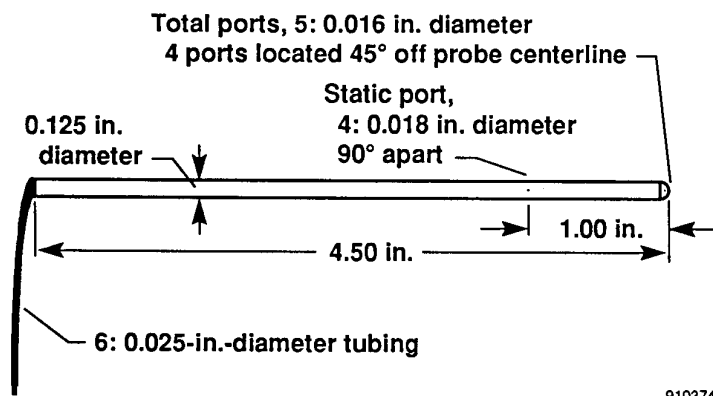


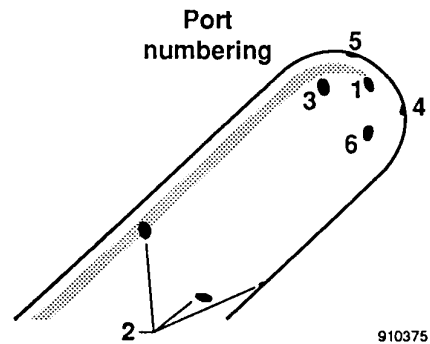
Figure 1. NASA F-18 HARV.

EC89 0062-001



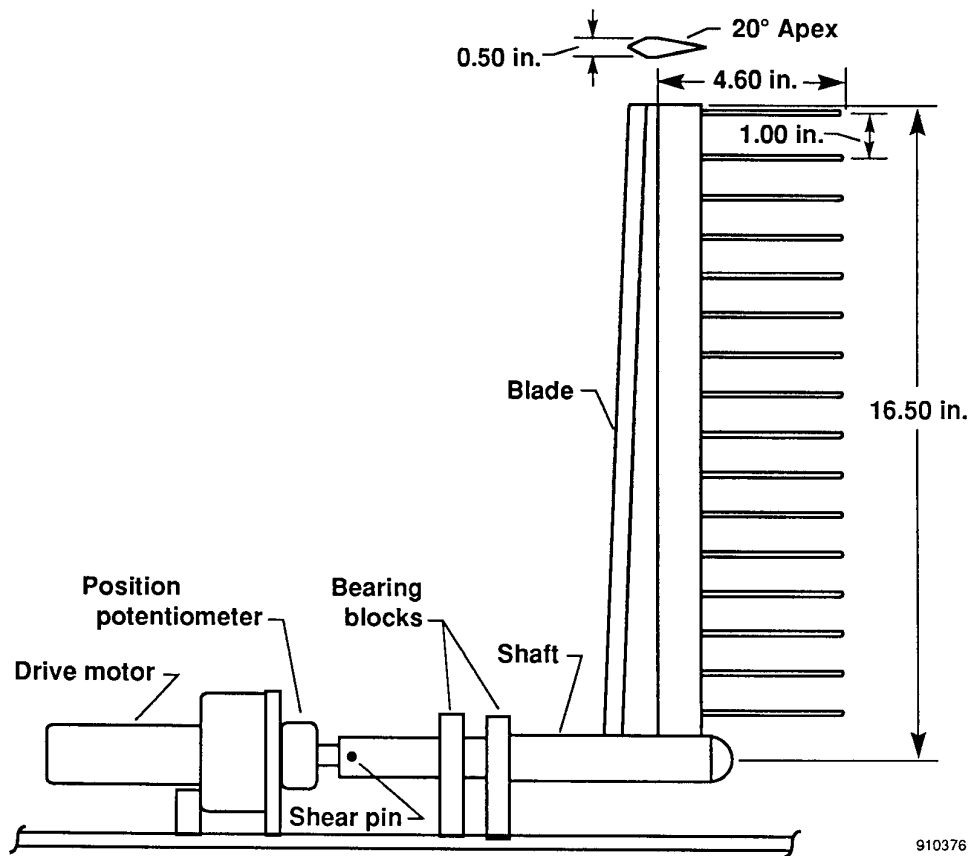
(a) Hemispherical-tipped five-hole probe.

910374



910375

(b) Five-hole probe nomenclature.



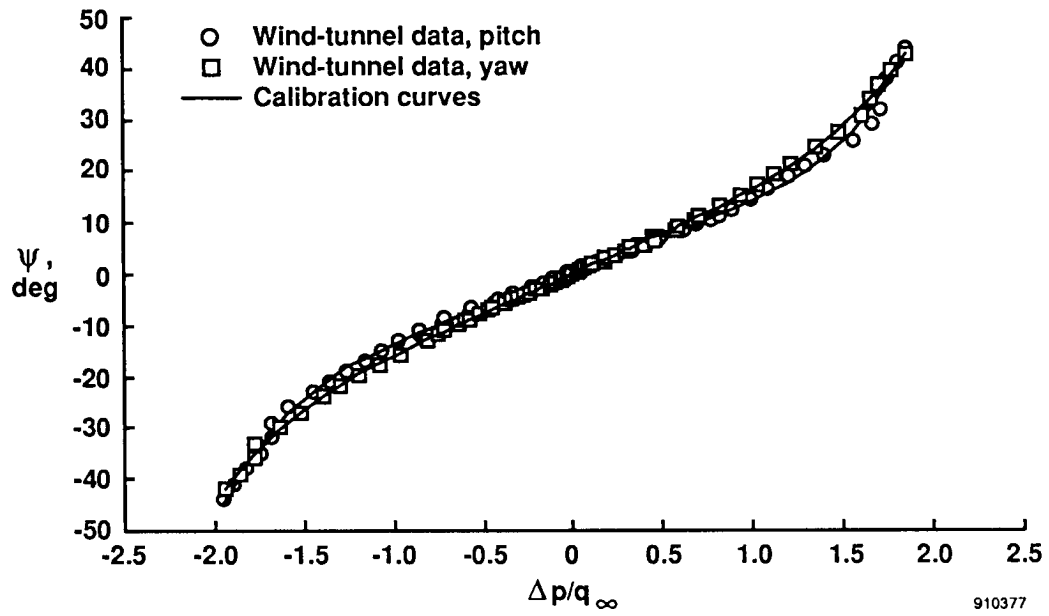
(c) Survey rake.

Figure 2. LEX survey rake.

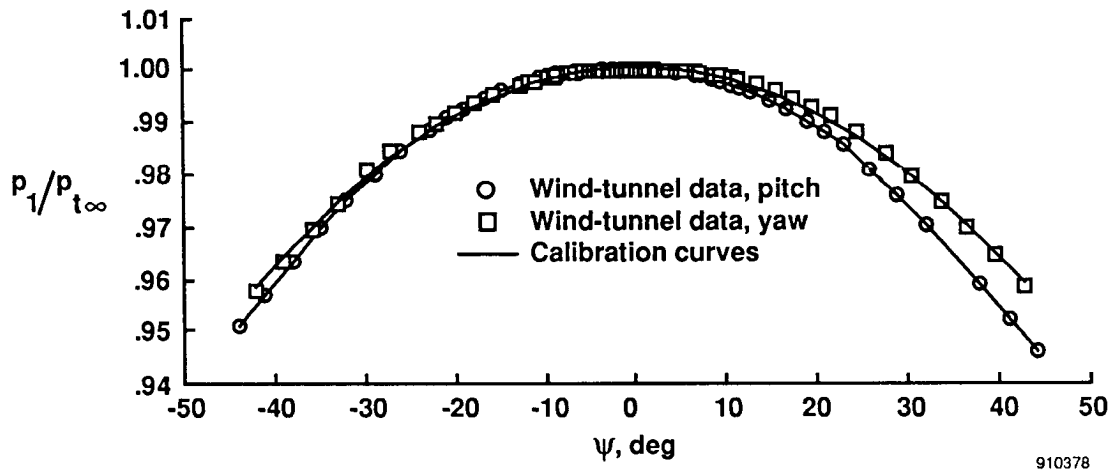


EC89 0235-002

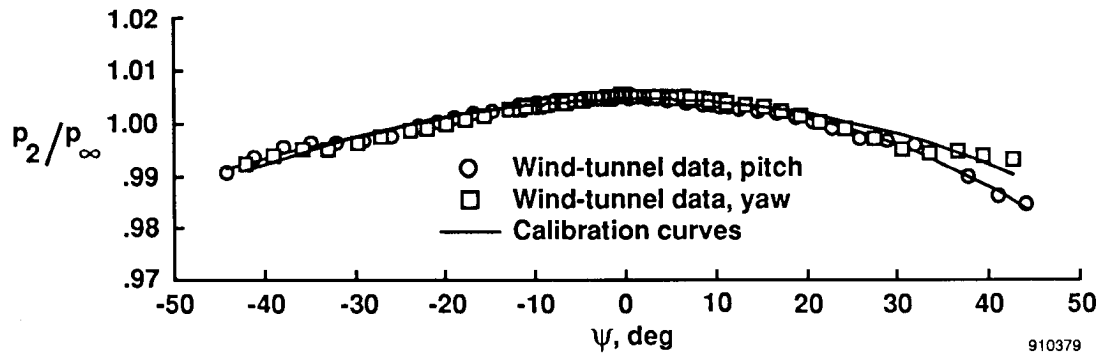
Figure 3. LEX survey rake located on the upper surface of the right LEX with the probe tips located at F.S. 253.



(a) Flow angularity.



(b) Total pressure.



(c) Static pressure.

Figure 4. Typical calibration data sets.

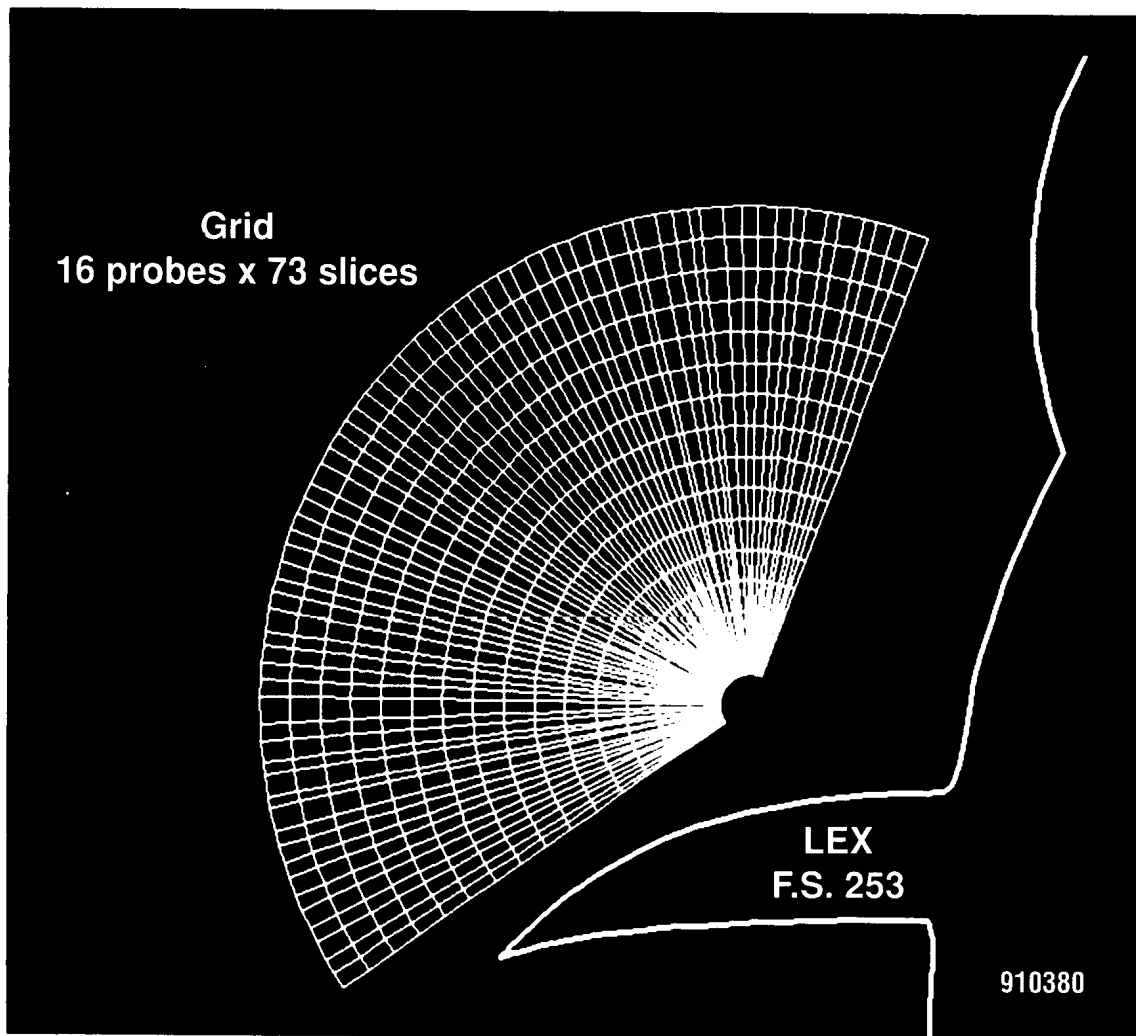
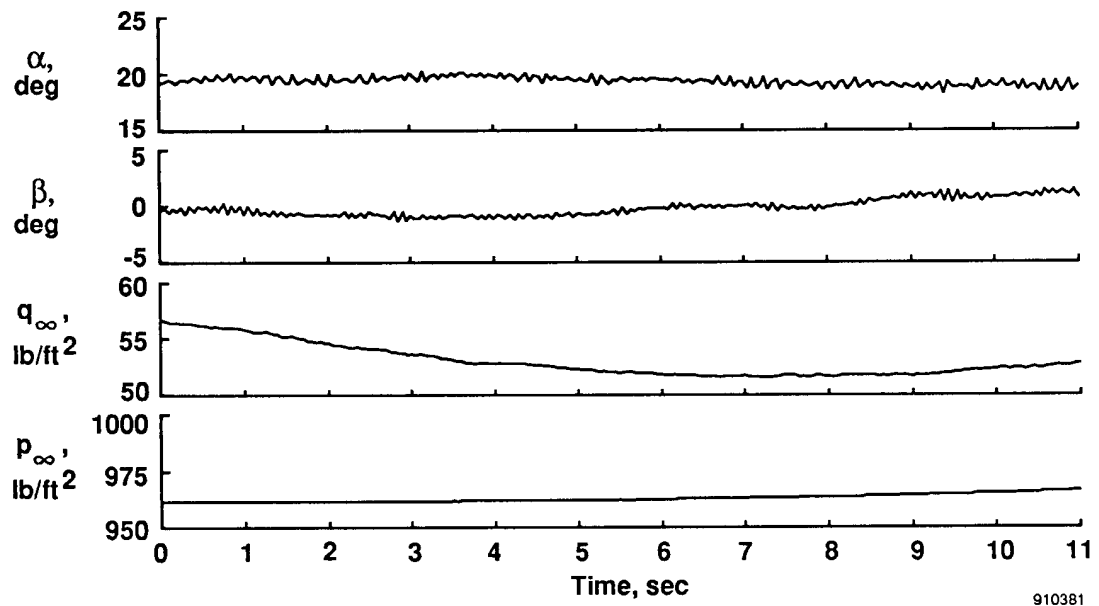
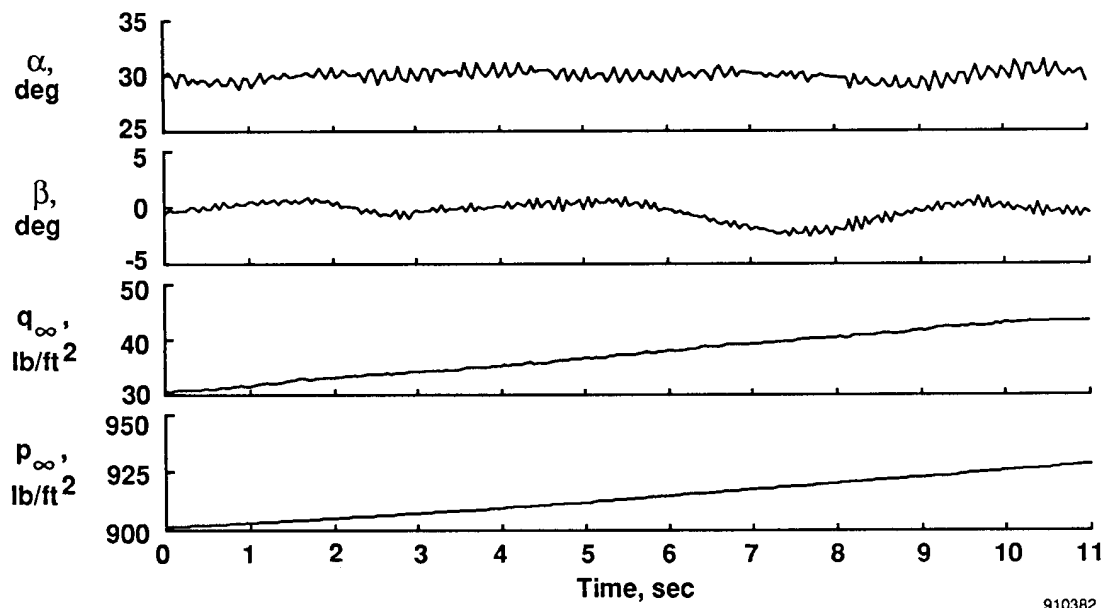


Figure 5. Grid of measured data points.



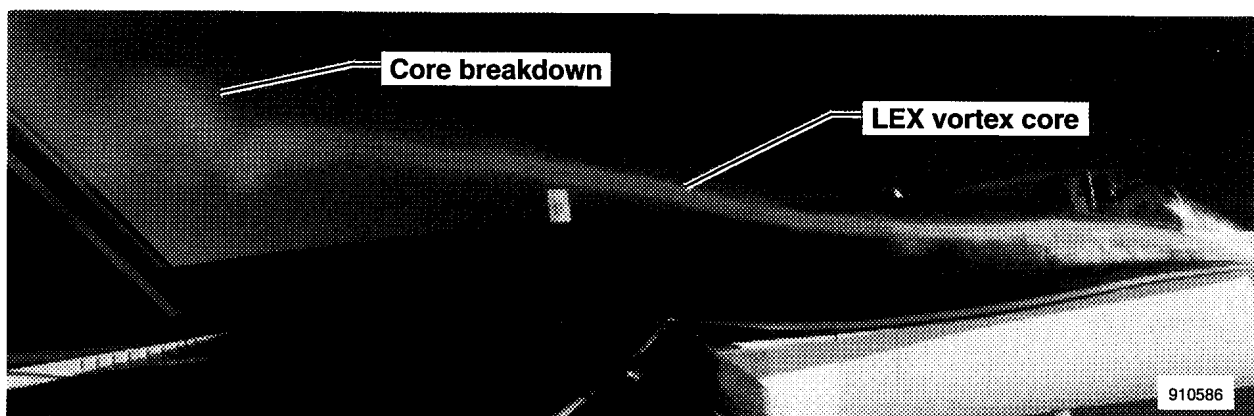


(a)  $\alpha = 19.4^\circ$ ,  $\beta = -0.2^\circ$ ,  $M = 0.28$ .

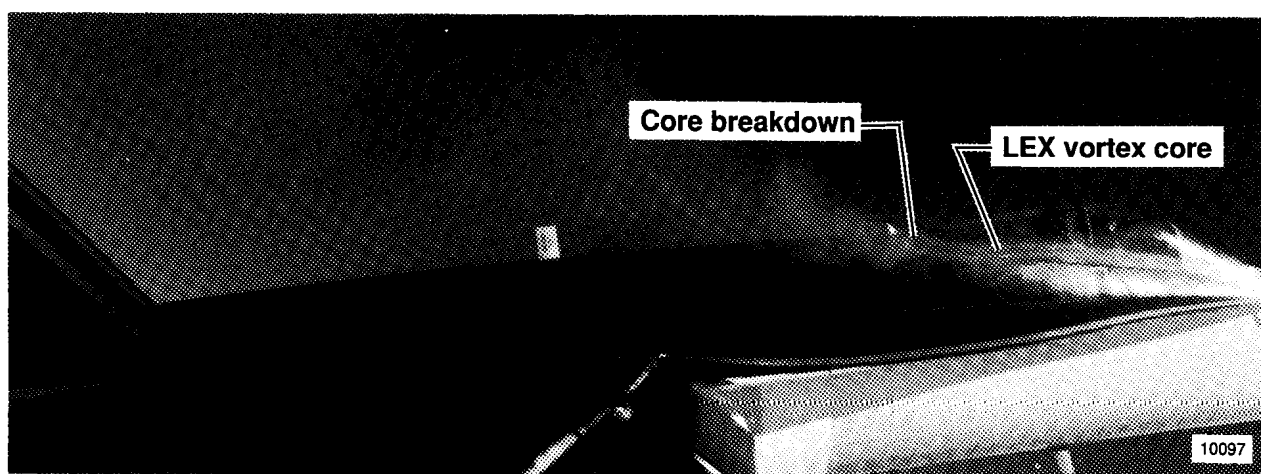


(b)  $\alpha = 30.0^\circ$ ,  $\beta = -0.3^\circ$ ,  $M = 0.24$ .

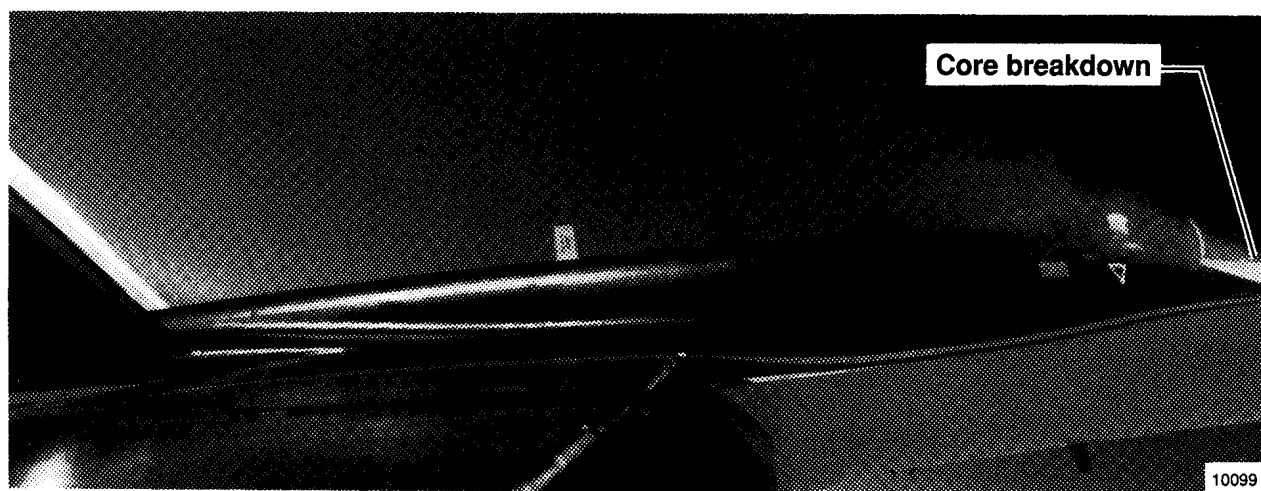
Figure 6. History of F-18 HARV during flight test.



(a)  $\alpha = 20.0^\circ$ ,  $\beta = 0.0^\circ$ .

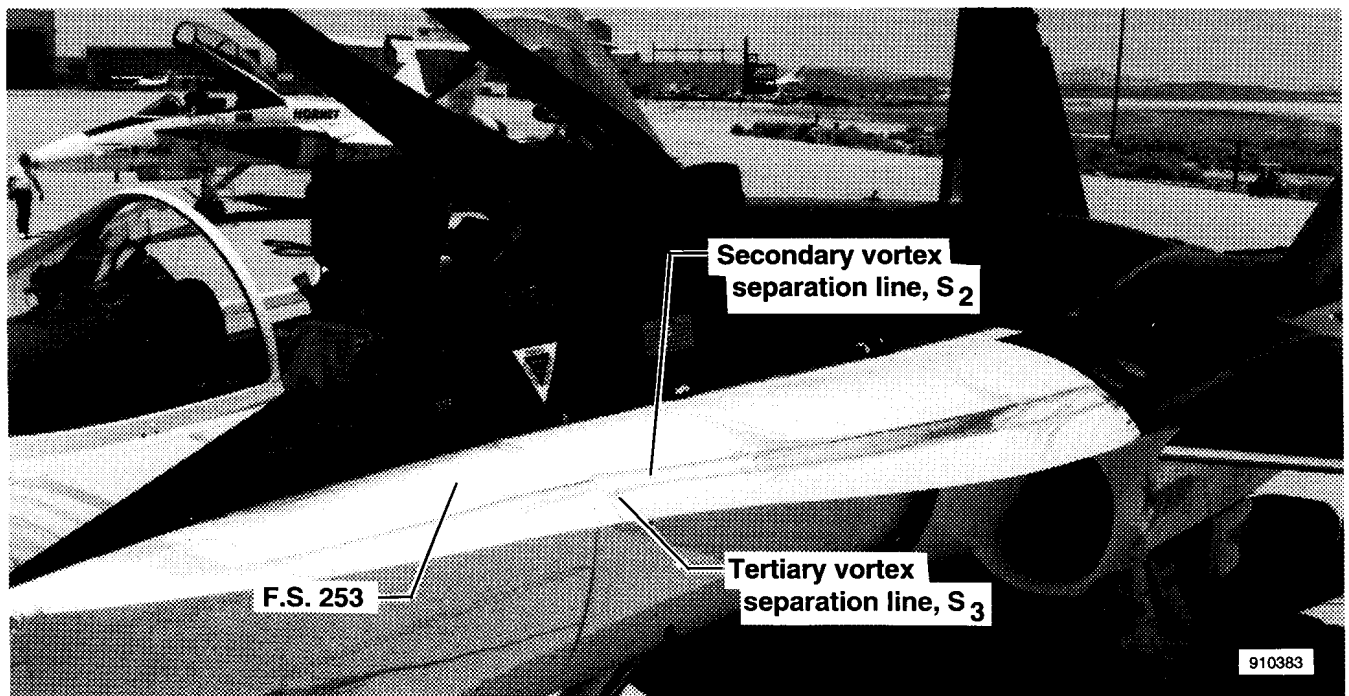


(b)  $\alpha = 29.8^\circ$ ,  $\beta = 0.2^\circ$ .

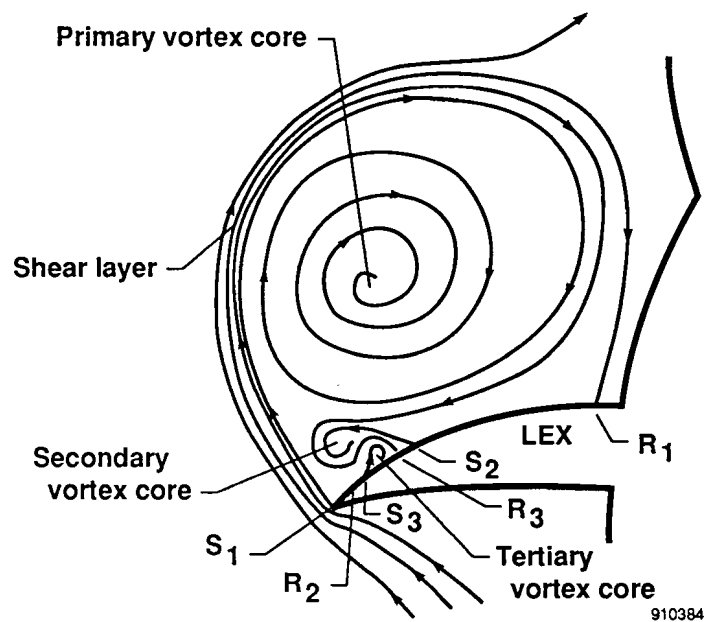


(c)  $\alpha = 42.5^\circ$ ,  $\beta = 0.8^\circ$ .

Figure 7. View from wingtip of LEX vortex core and core breakdown (ref. 20).



(a) Surface flow visualization on the F-18 HARV left LEX,  $\alpha \approx 30^\circ$ , (ref. 22).



(b) Schematic of crossflow about LEX.

Figure 8. F-18 LEX flow field.

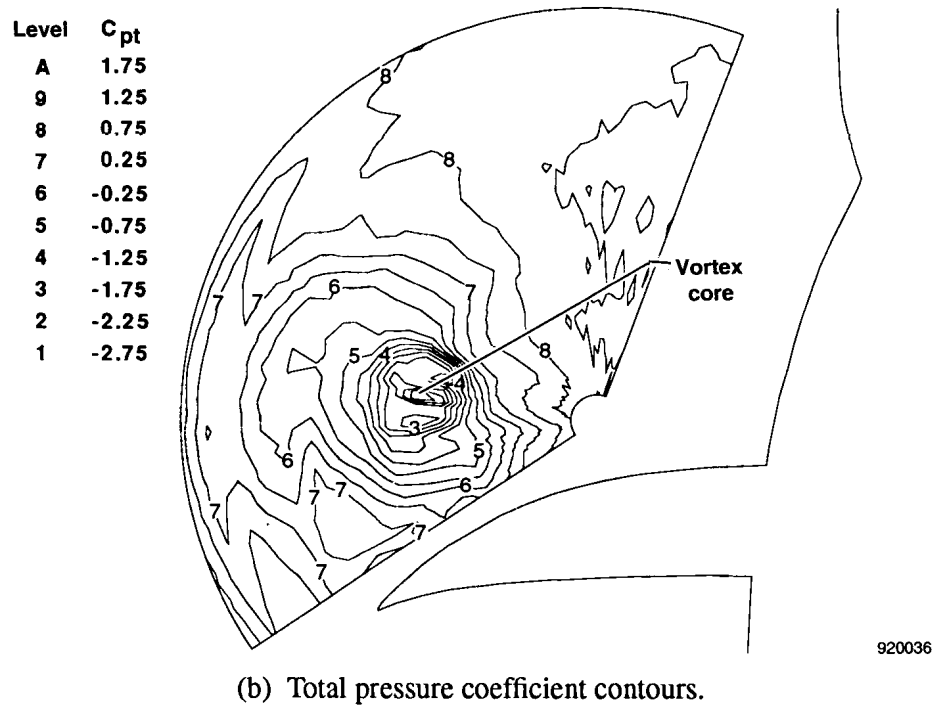
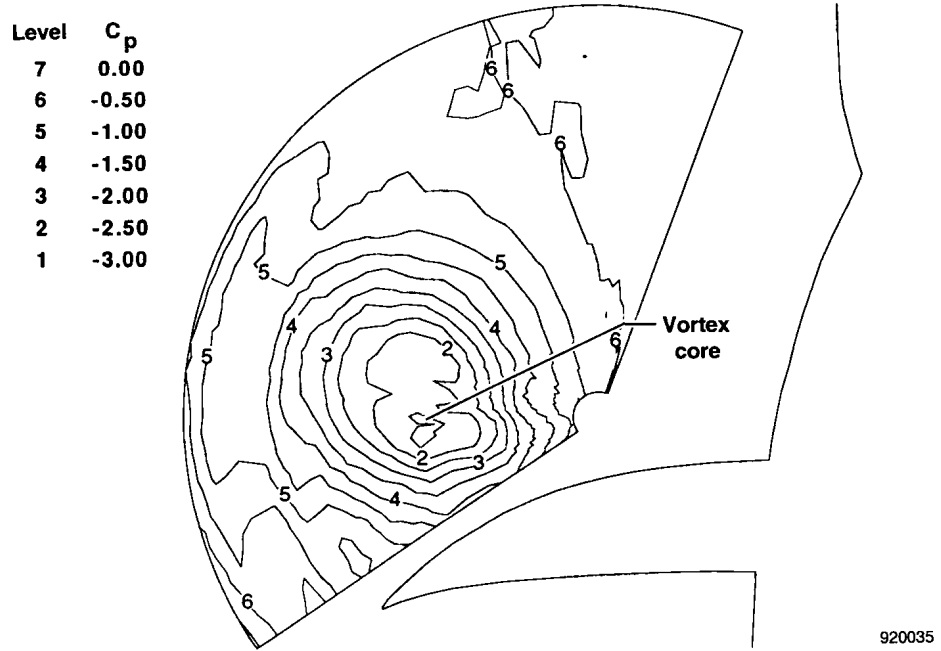
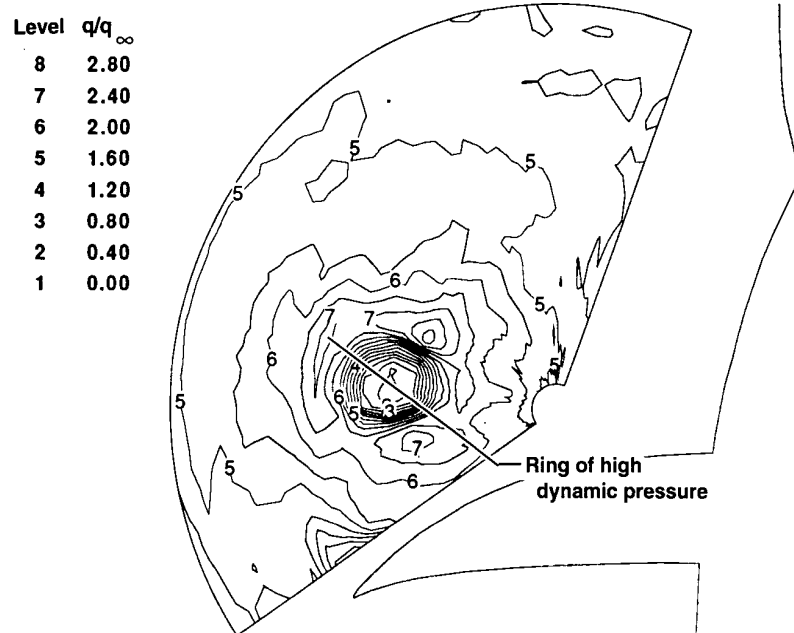
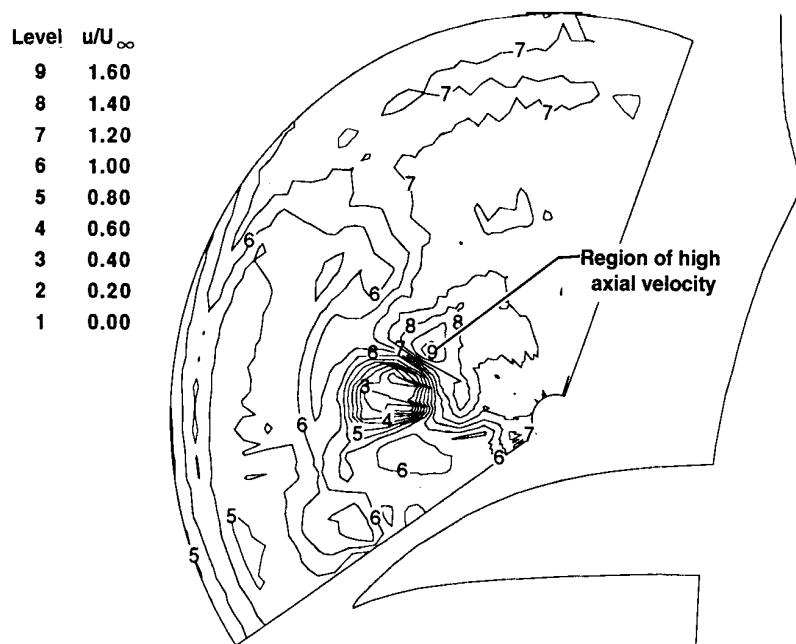


Figure 9. LEX vortex flow-field measurements;  $\alpha \approx 19^\circ$ ,  $\beta \approx -0.2^\circ$ ,  $M \approx 0.28$ ,  $Re \approx 12.0 \times 10^6$ .



920037

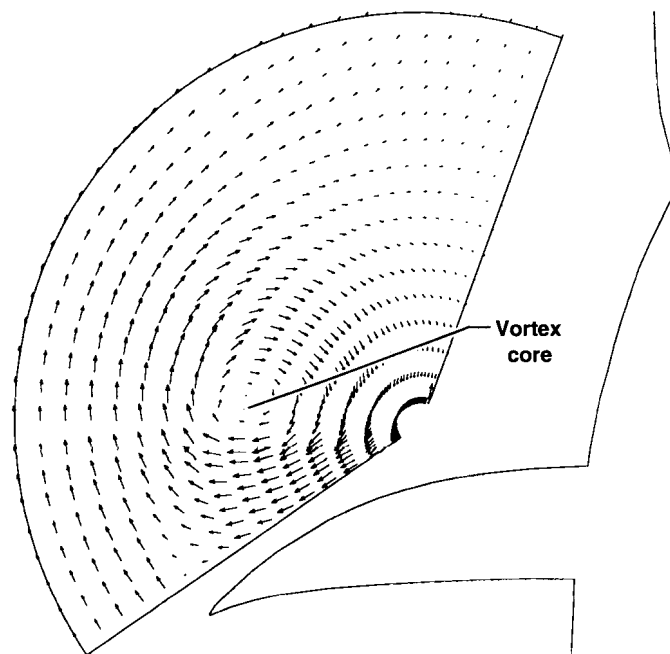
(c) Normalized dynamic pressure contours.



920038

(d) Normalized axial velocity contours.

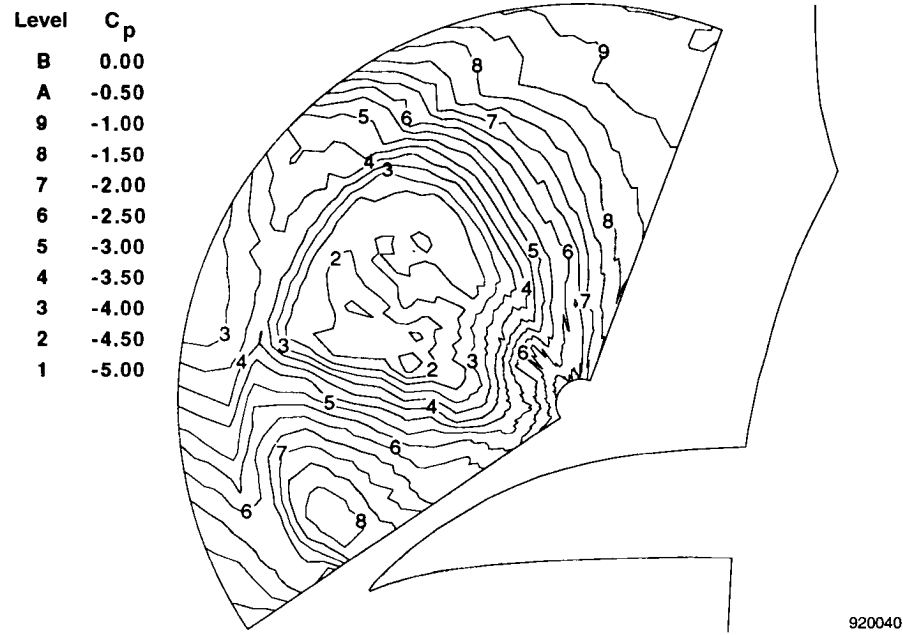
Figure 9. Continued.



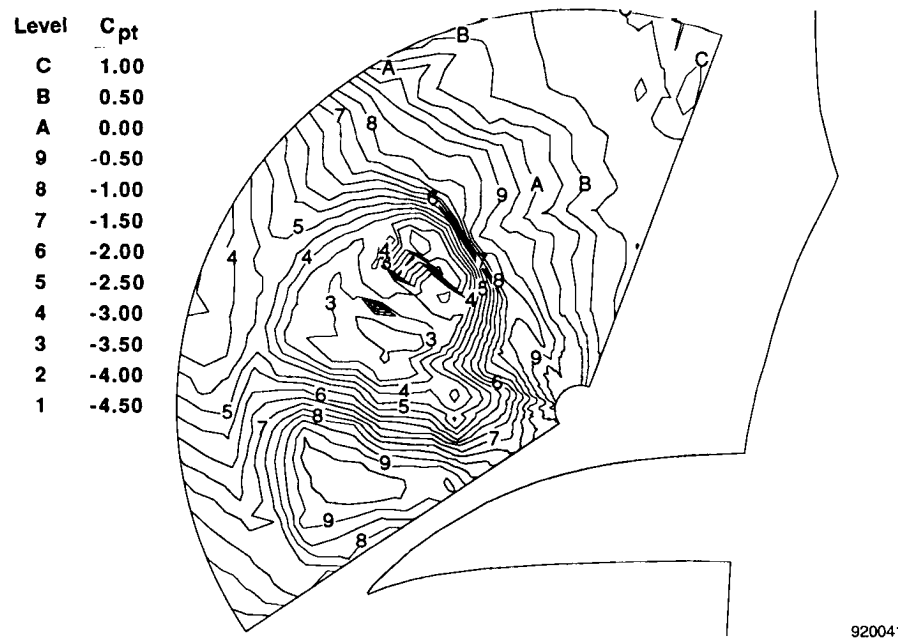
920039

(e) Normalized crossflow velocity vectors.

Figure 9. Concluded.



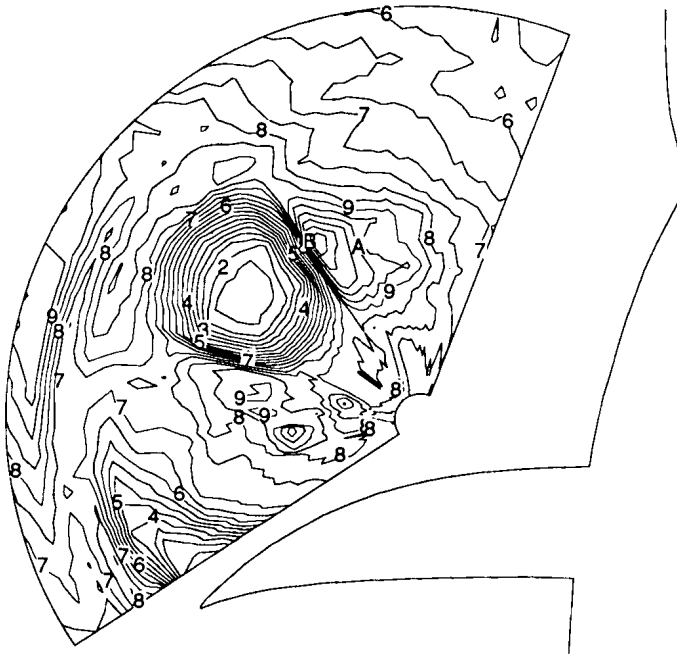
(a) Static pressure coefficient contours.



(b) Total pressure coefficient contours.

Figure 10. LEX vortex flow-field measurements;  $\alpha \approx 30^\circ$ ,  $\beta \approx -0.3^\circ$ ,  $M \approx 0.24$ ,  $Re \approx 9.4 \times 10^6$ .

Level	$q/q_\infty$
C	4.40
B	4.00
A	3.60
9	3.20
8	2.80
7	2.40
6	2.00
5	1.60
4	1.20
3	0.80
2	0.40
1	0.00



920042

(c) Normalized dynamic pressure contours.

Level	$u/U_\infty$
B	2.00
A	1.80
9	1.60
8	1.40
7	1.20
6	1.00
5	0.80
4	0.60
3	0.40
2	0.20
1	0.00

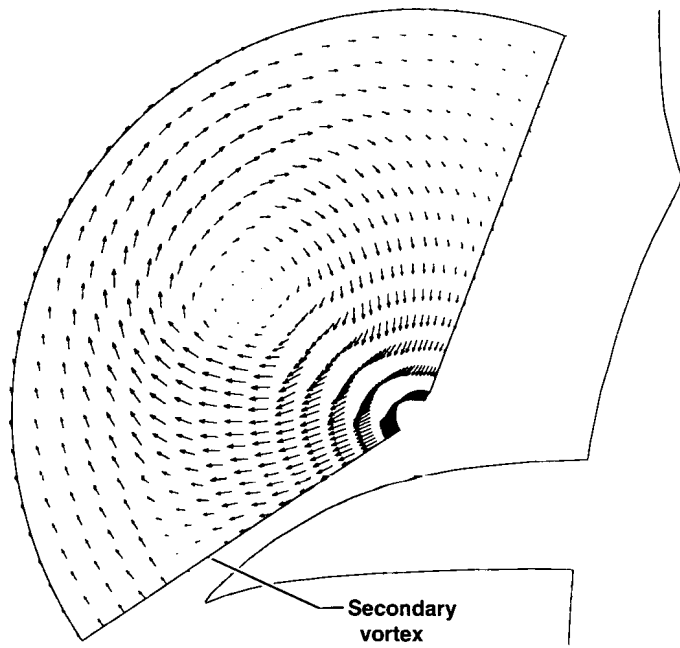


920043

(d) Normalized axial velocity contours.

Figure 10. Continued.



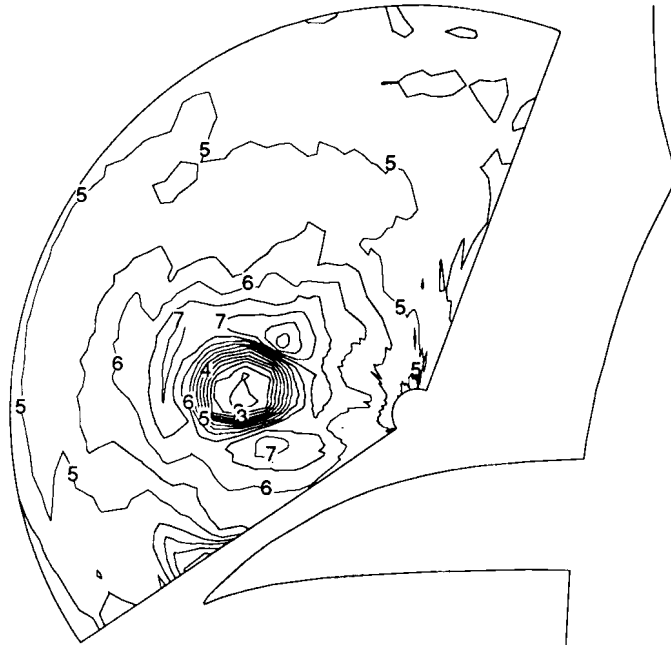


920044

(e) Normalized crossflow velocity vectors.

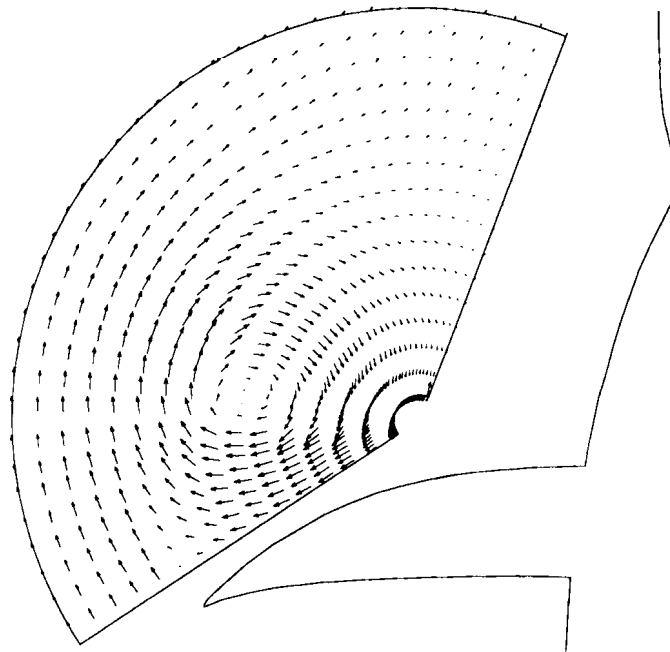
Figure 10. Concluded.

Level	$q/q_\infty$
8	2.80
7	2.40
6	2.00
5	1.60
4	1.20
3	0.80
2	0.40
1	0.00



920045

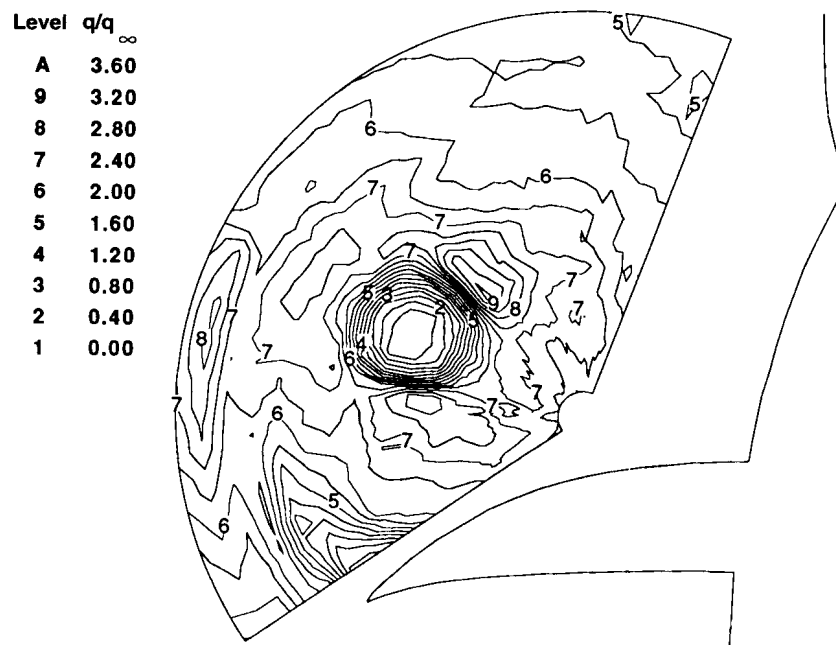
(a) Normalized dynamic pressure contours,  $\alpha \approx 19^\circ$ .



920046

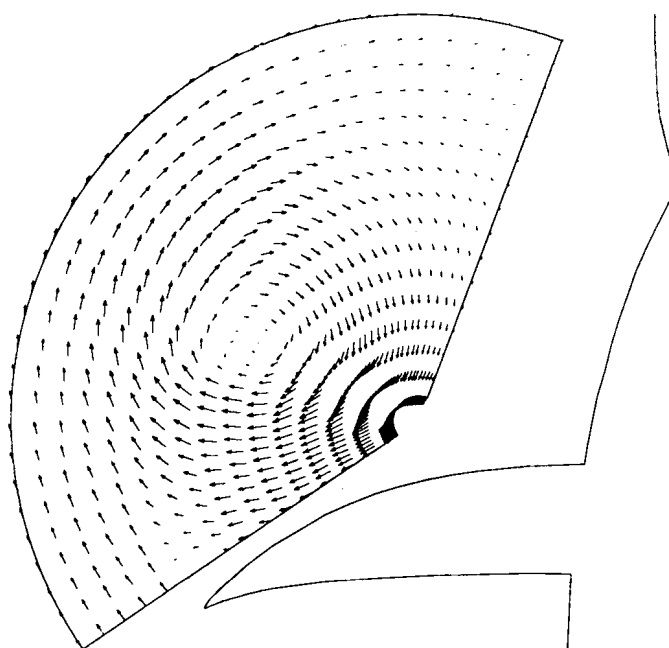
(b) Crossflow velocity vectors,  $\alpha \approx 19^\circ$ .

Figure 11. Effect of angle of attack on LEX.



920047

(c) Normalized dynamic pressure contours,  $\alpha \approx 26^\circ$ .

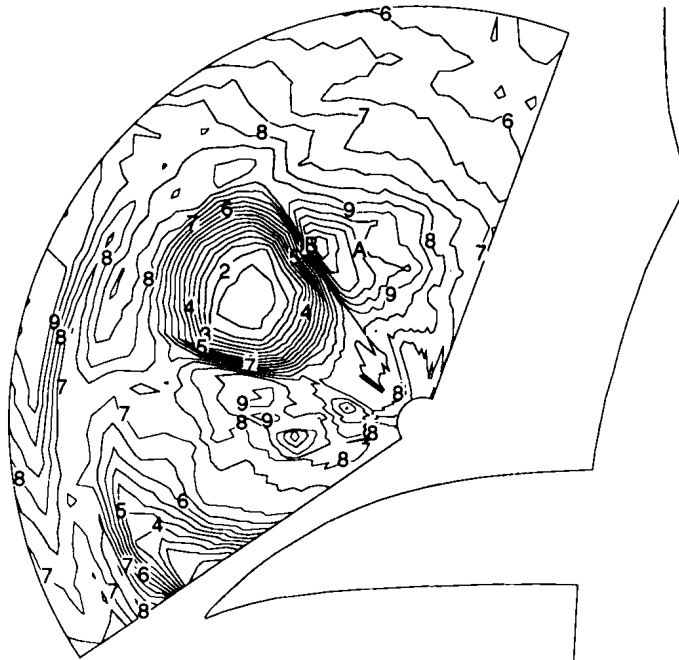


920048

(d) Crossflow velocity vectors,  $\alpha \approx 26^\circ$ .

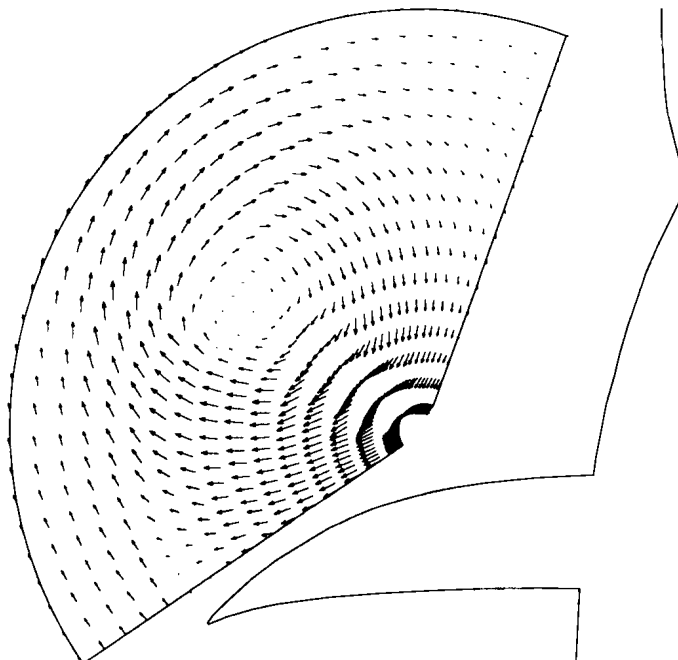
Figure 11. Continued.

Level	$q/q_\infty$
C	4.40
B	4.00
A	3.60
9	3.20
8	2.80
7	2.40
6	2.00
5	1.60
4	1.20
3	0.80
2	0.40
1	0.00



920049

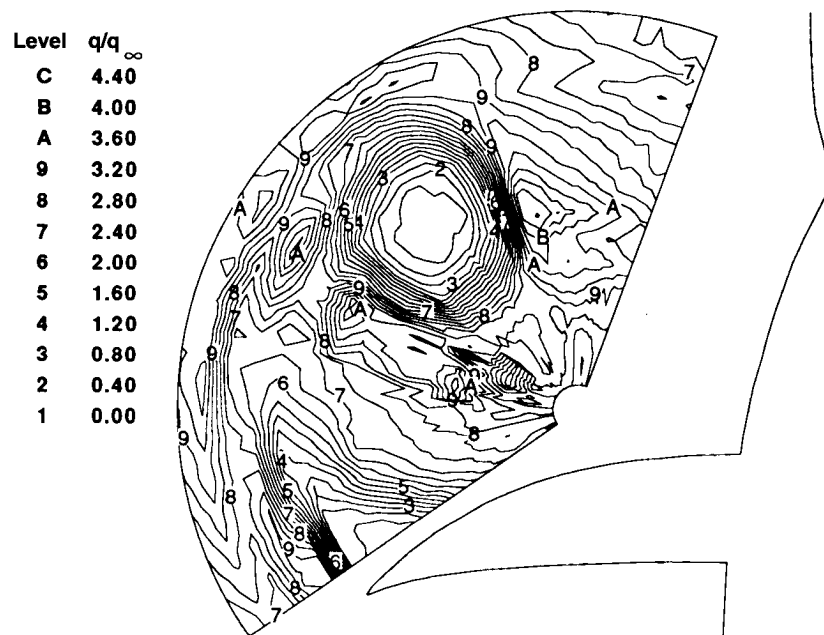
(e) Normalized dynamic pressure contours,  $\alpha \approx 30^\circ$ .



920050

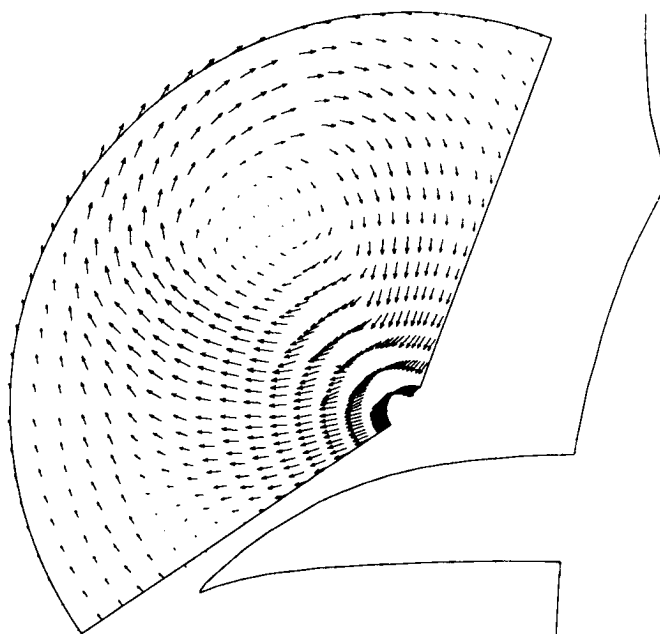
(f) Crossflow velocity vectors,  $\alpha \approx 30^\circ$ .

Figure 11. Continued.



920051

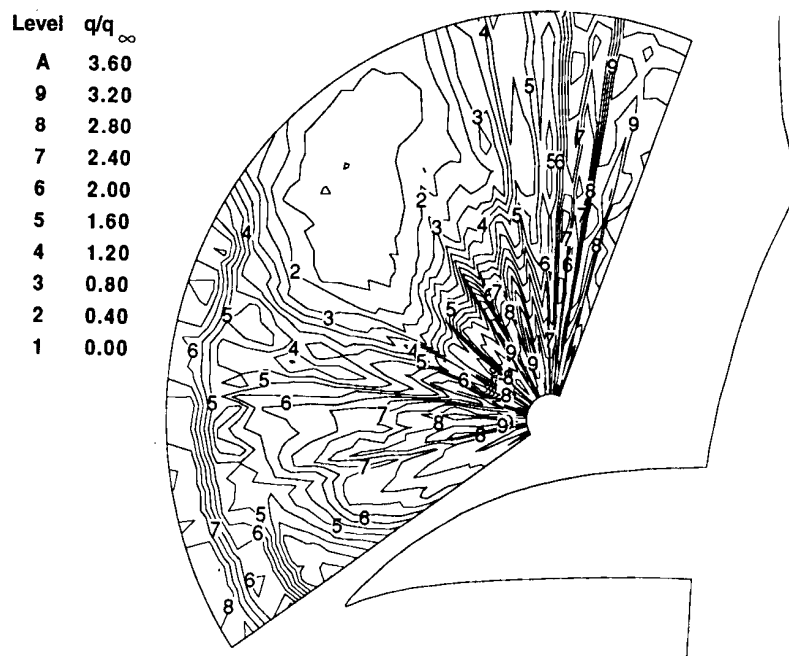
(g) Normalized dynamic pressure contours,  $\alpha \approx 36^\circ$ .



920052

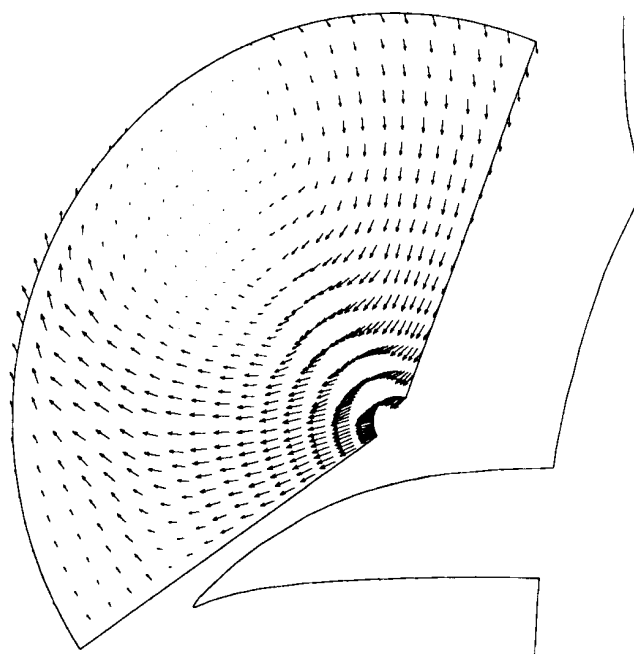
(h) Crossflow velocity vectors,  $\alpha \approx 36^\circ$ .

Figure 11. Continued.



920053

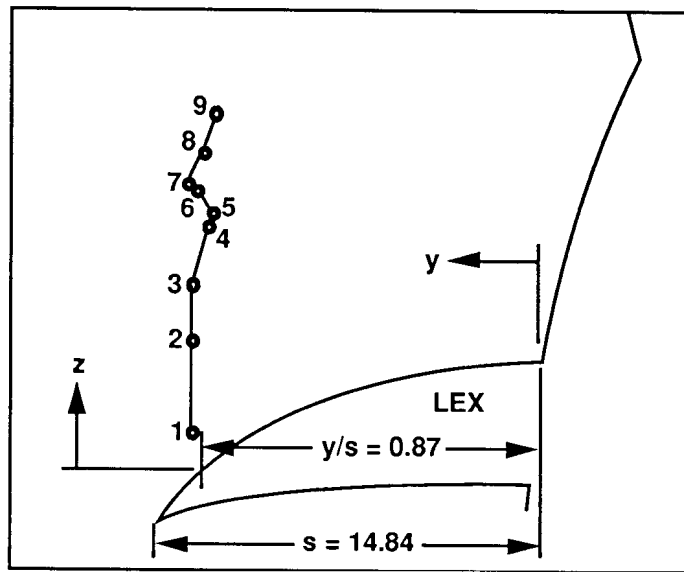
(i) Normalized dynamic pressure contours,  $\alpha \approx 48^\circ$ .



920054

(j) Crossflow velocity vectors,  $\alpha \approx 48^\circ$ .

Figure 11. Concluded.



Point	$\alpha$ , deg	y/s	z/s
1	9.7	0.90	0.08
2	15.4	0.90	0.30
3	19.4	0.90	0.43
4	23.0	0.86	0.57
5	25.5	0.85	0.61
6	28.1	0.89	0.66
7	30.0	0.91	0.68
8	34.2	0.87	0.76
9	35.9	0.84	0.86

920077

Figure 12. Effect of angle of attack on LEX vortex core location.

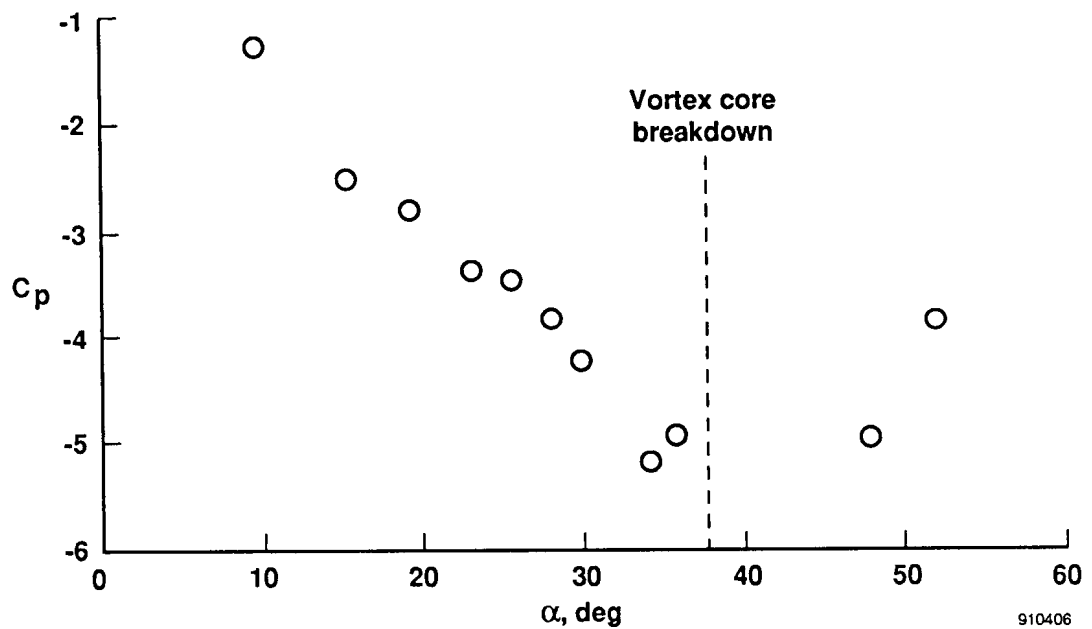


Figure 13. Minimum static pressure coefficients in LEX vortex core as a function of angle of attack.

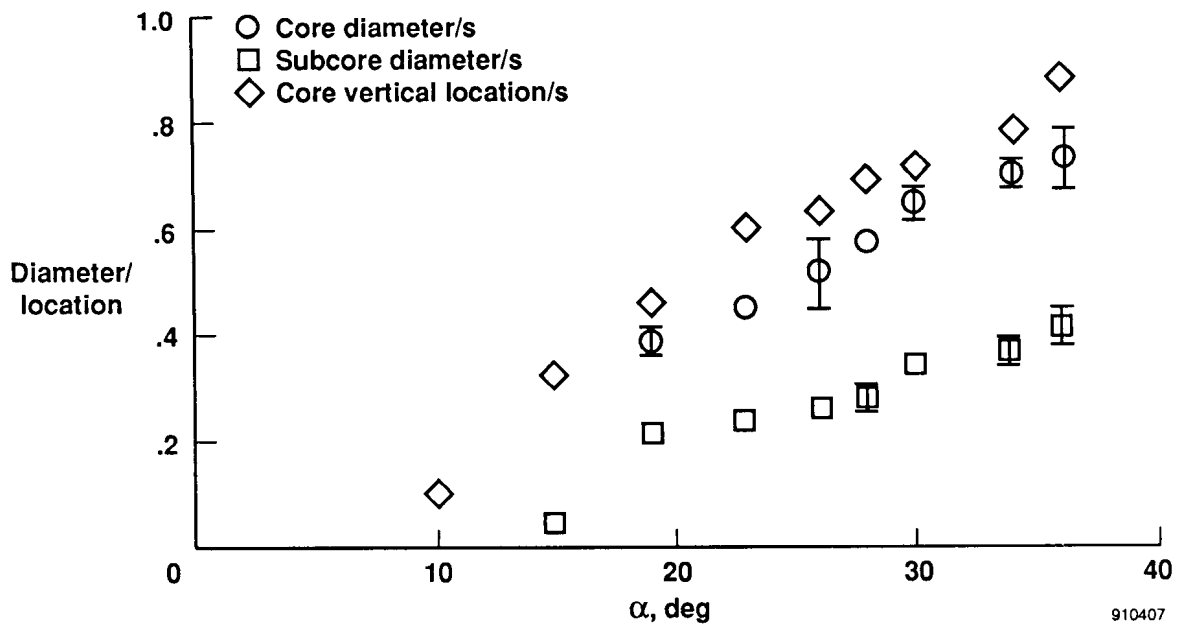
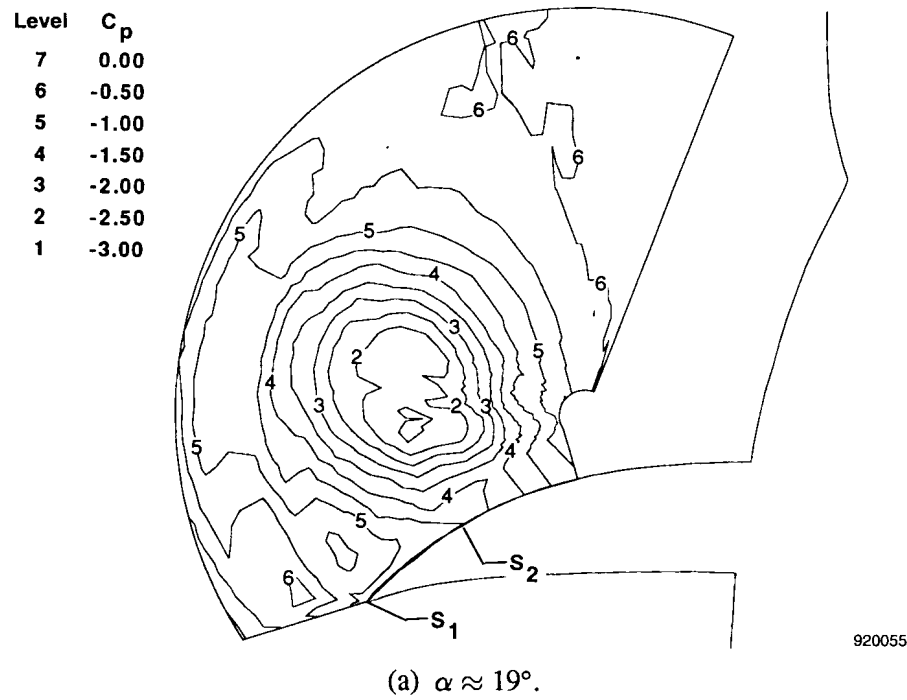
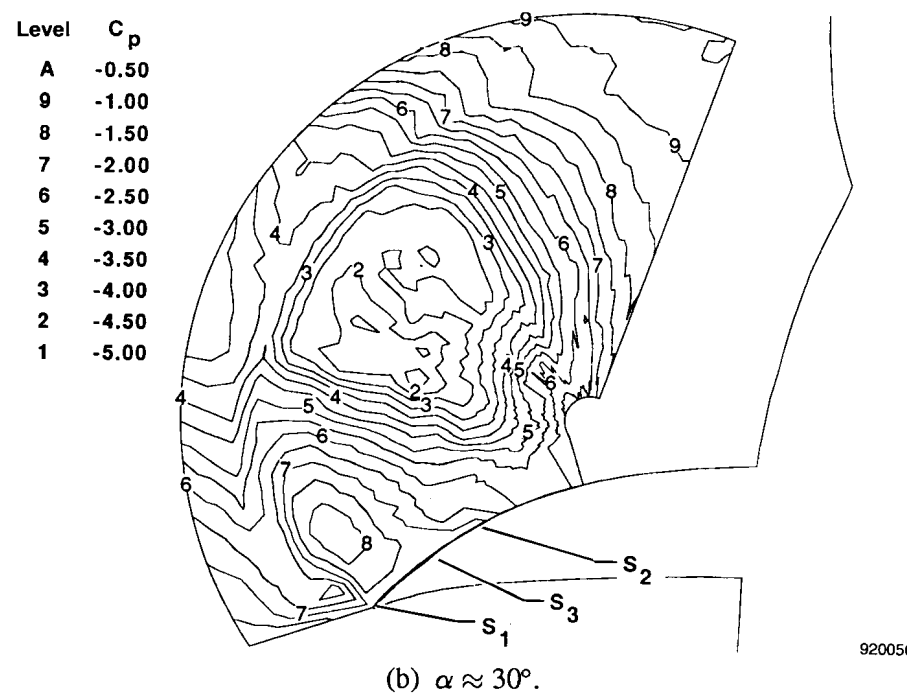


Figure 14. Effect of angle of attack on nondimensionalized LEX vortex core diameter and vertical location.



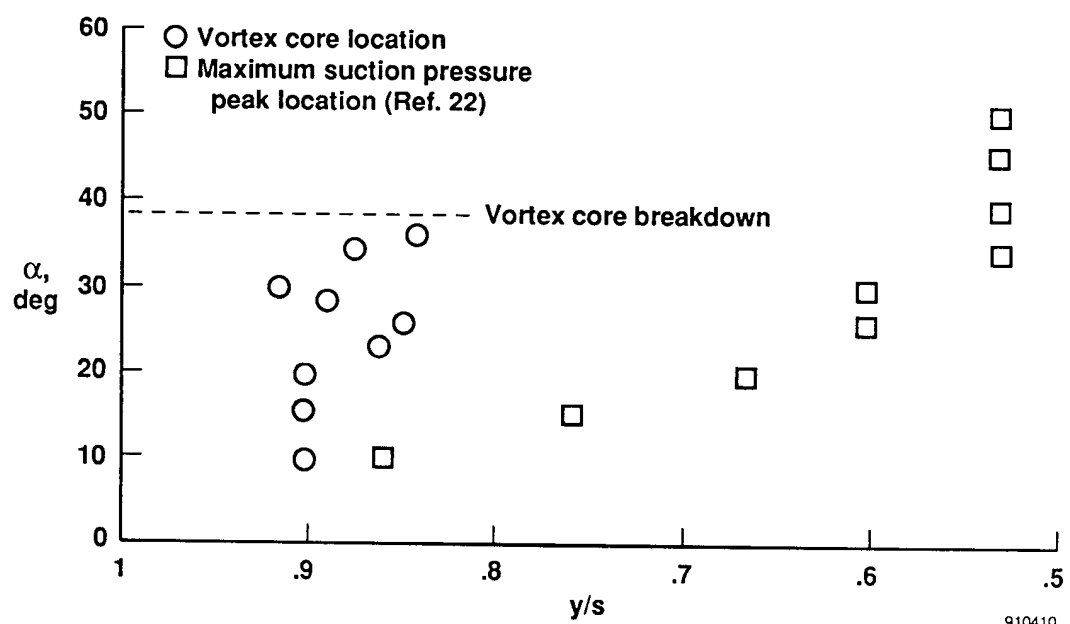


920055



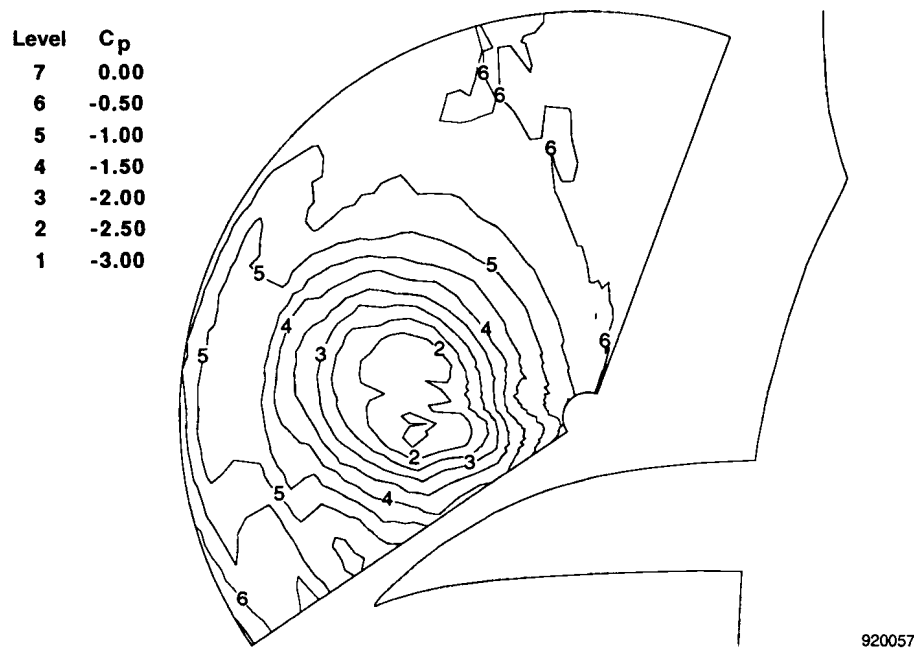
920056

Figure 15. Off-surface LEX vortex static pressure coefficient contours and comparison to surface static pressure coefficient distributions and on-surface flow visualization results.

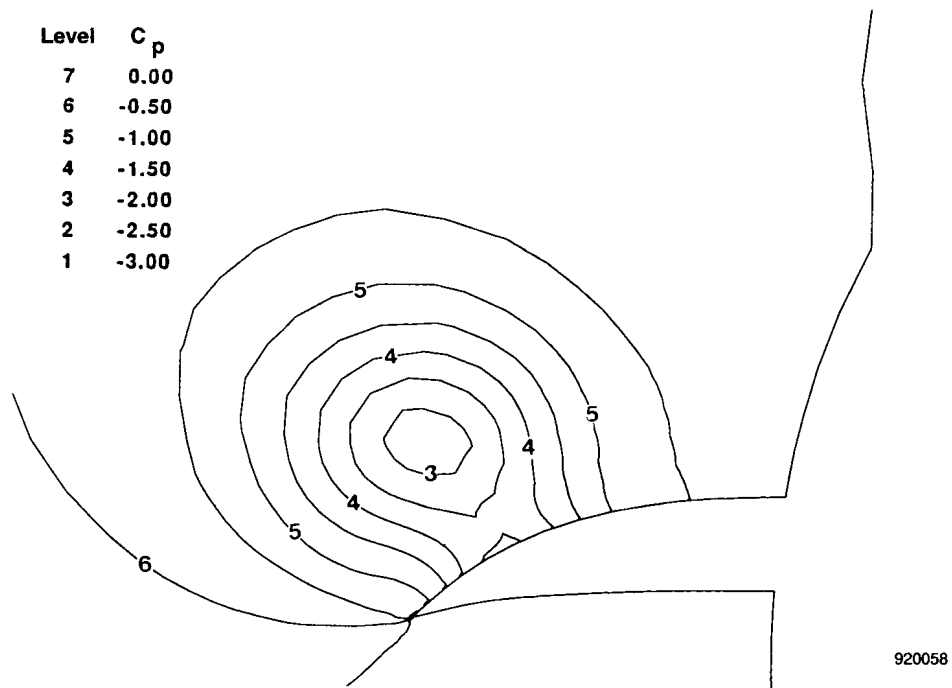


910410

Figure 16. Lateral position of vortex core and maximum suction pressure peak location as a function of angle of attack.



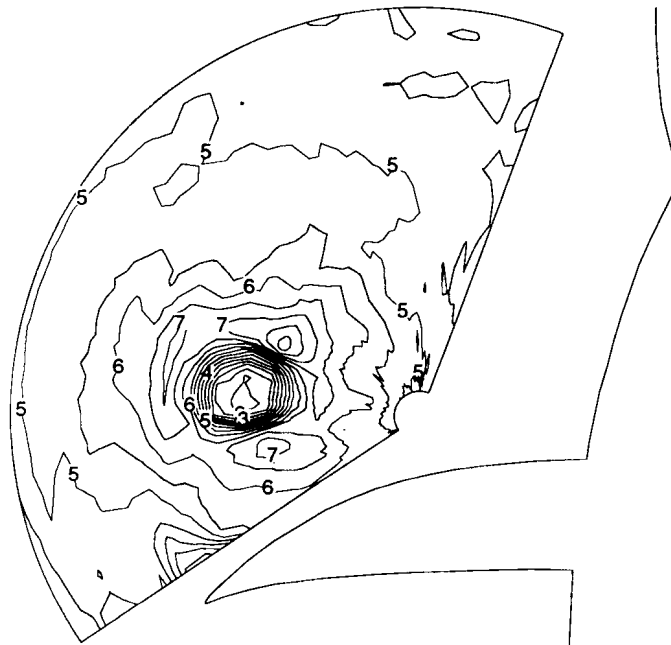
(a) Static pressure coefficient contours, flight data.



(b) Static pressure coefficient contours, computational solution.

Figure 17. LEX vortex flow-field measurements and comparison to computational solutions,  $\alpha \approx 19^\circ$ .

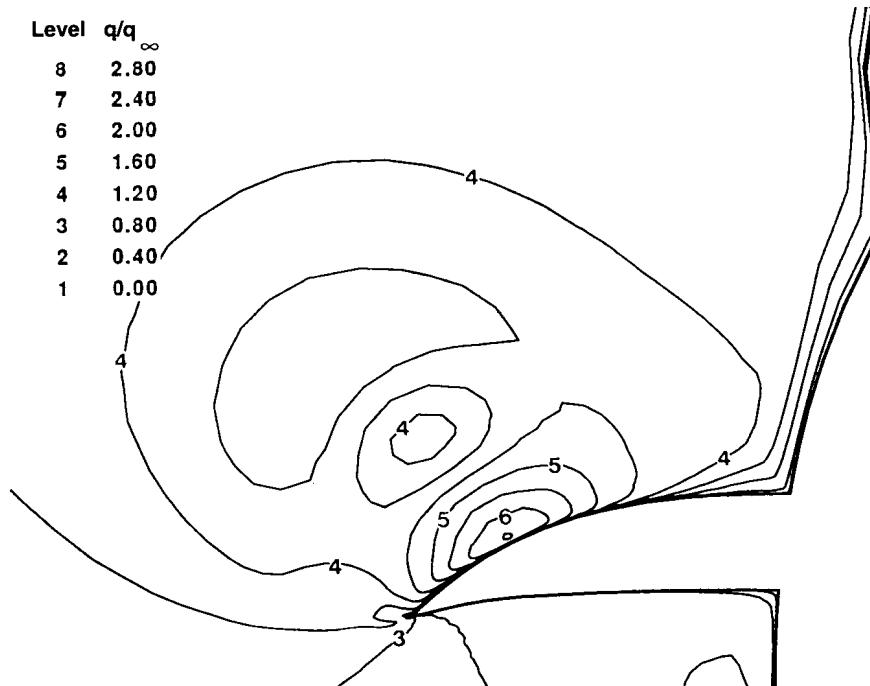
Level	$q/q_\infty$
8	2.80
7	2.40
6	2.00
5	1.60
4	1.20
3	0.80
2	0.40
1	0.00



920059

(c) Dynamic pressure contours flight data.

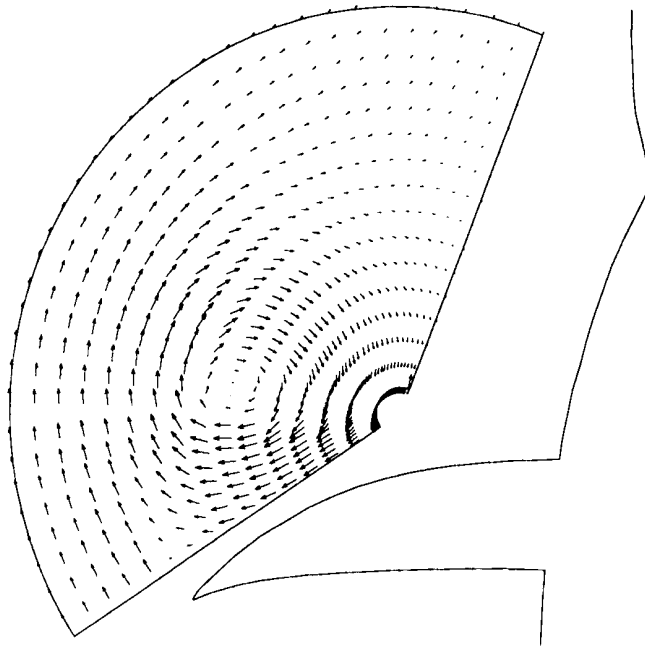
Level	$q/q_\infty$
8	2.80
7	2.40
6	2.00
5	1.60
4	1.20
3	0.80
2	0.40
1	0.00



920060

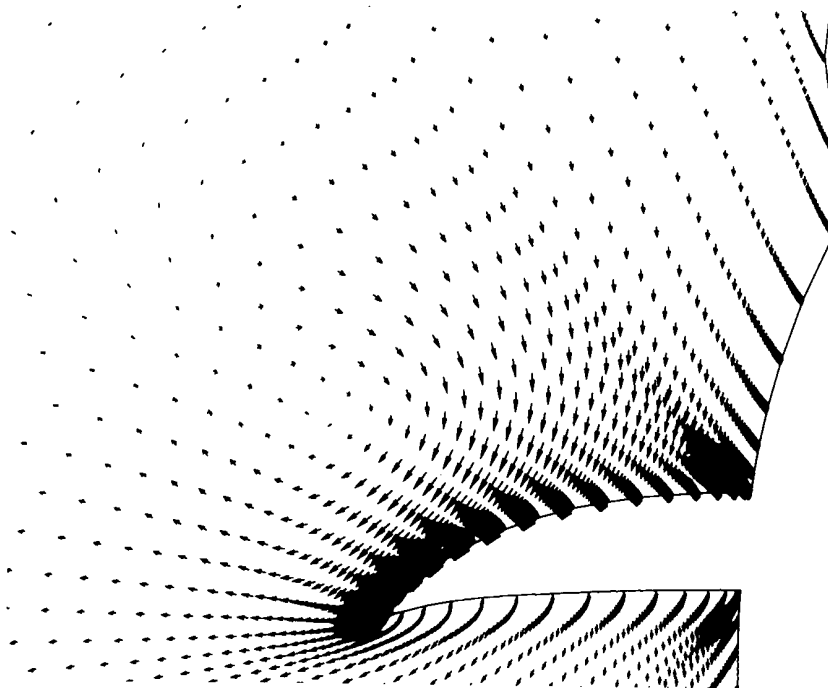
(d) Dynamic pressure contours, computational solution.

Figure 17. Continued.



920061

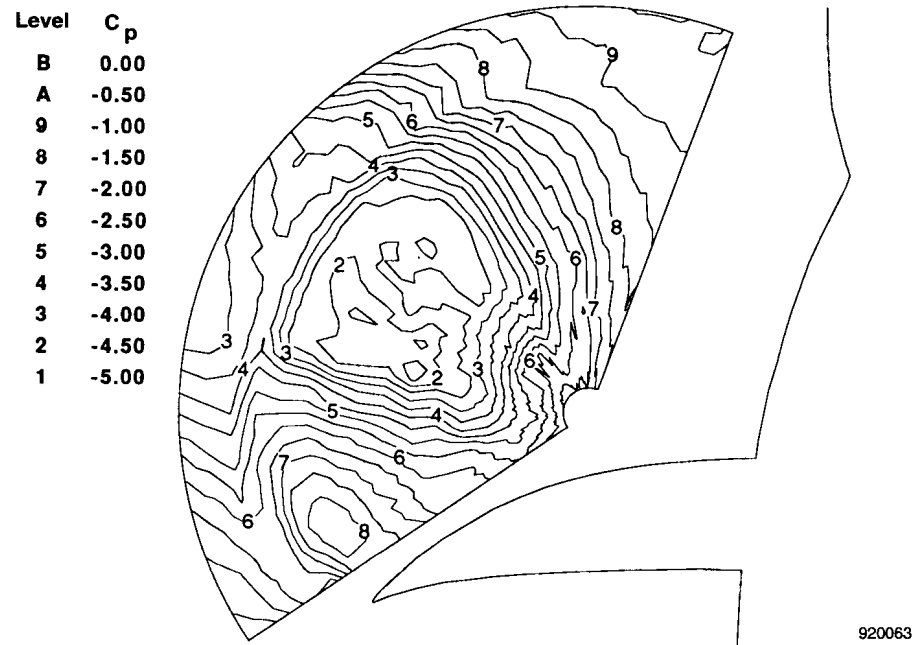
(e) Crossflow velocity vectors, flight data.



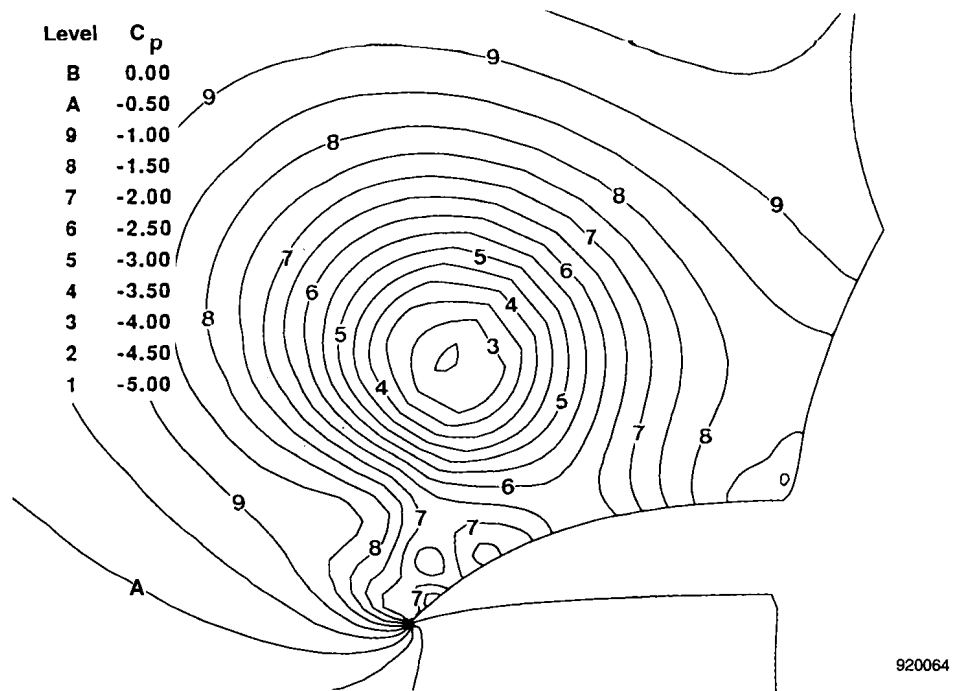
920062

(f) Crossflow velocity vectors, computational solution.

Figure 17. Concluded.

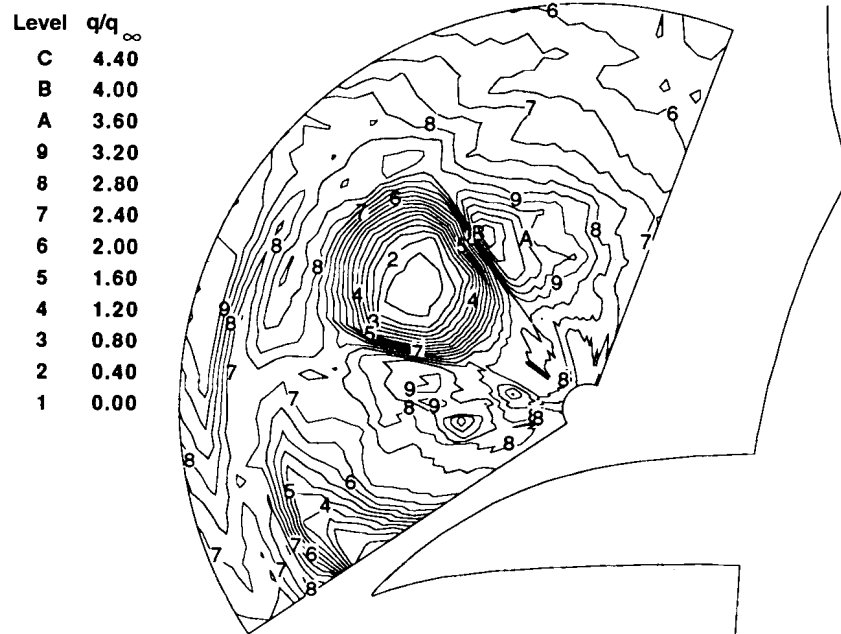


(a) Static pressure coefficient contours, flight data.



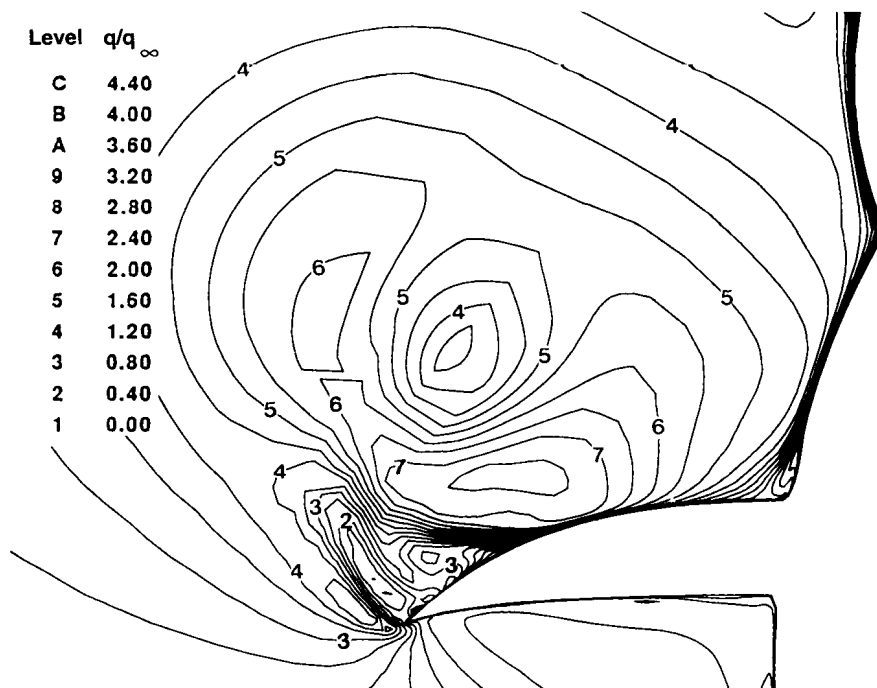
(b) Static pressure coefficient contours, computational solution.

Figure 18. LEX vortex flow-field measurements and comparison to computational solutions,  $\alpha \approx 30^\circ$ .



920065

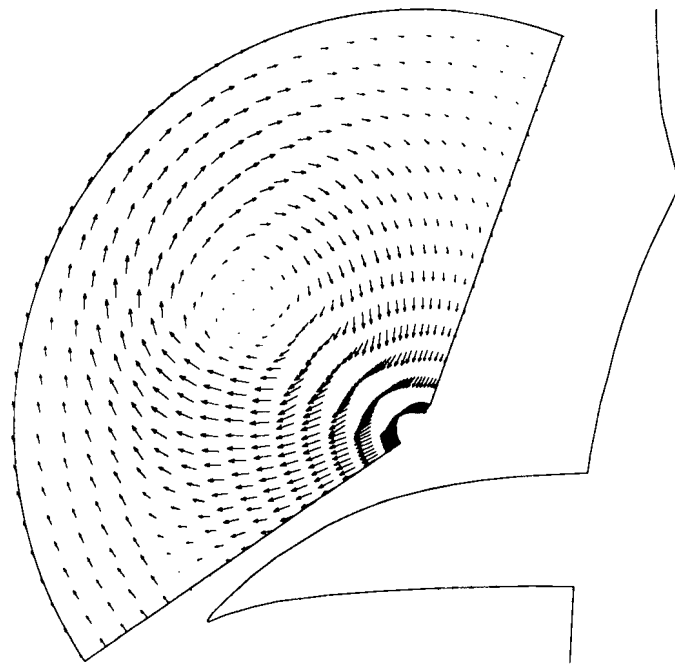
(c) Dynamic pressure contours, flight data.



920066

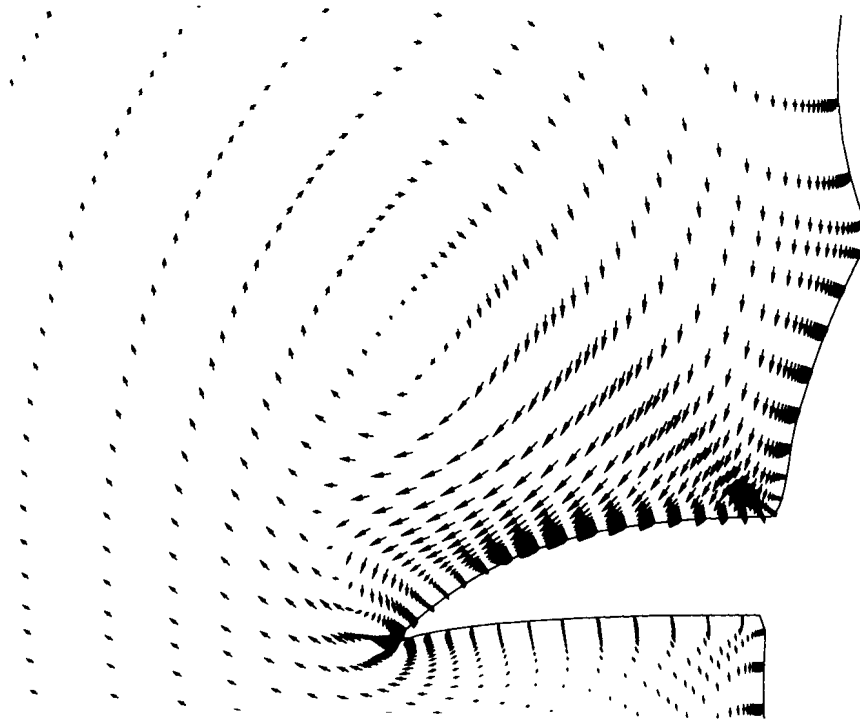
(d) Dynamic pressure contours, computational solution.

Figure 18. Continued.



920067

(e) Crossflow velocity vectors, flight data.



920068

(f) Crossflow velocity vectors, computational solution.

Figure 18. Concluded.



REPORT DOCUMENTATION PAGE			Form Approved OMB No. 0704-0188	
<small>Public reporting burden for this collection of information is estimated to average 1 hour per response, including the time for reviewing instructions, searching existing data sources, gathering and maintaining the data needed, and completing and reviewing the collection of information. Send comments regarding this burden estimate or any other aspect of this collection of information, including suggestions for reducing this burden, to Washington Headquarters Services, Directorate for Information Operations and Reports, 1215 Jefferson Davis Highway, Suite 1204, Arlington, VA 22202-4302, and to the Office of Management and Budget, Paperwork Reduction Project (0704-0188), Washington, DC 20503.</small>				
1. AGENCY USE ONLY (Leave blank)	2. REPORT DATE September 1992	3. REPORT TYPE AND DATES COVERED Technical Memorandum		
4. TITLE AND SUBTITLE In-Flight Leading-Edge Extension Vortex Flow-Field Survey Measurements on a F-18 Aircraft at High Angle of Attack		5. FUNDING NUMBERS  WU-505-68-71		
6. AUTHOR(S) David M. Richwine (PRC Inc., Edwards, California) David F. Fisher (Dryden Flight Research Facility, Edwards, California)				
7. PERFORMING ORGANIZATION NAME(S) AND ADDRESS(ES) NASA Dryden Flight Research Facility P.O. Box 273 Edwards, California 93523-0273		8. PERFORMING ORGANIZATION REPORT NUMBER  H-1783		
9. SPONSORING/MONITORING AGENCY NAME(S) AND ADDRESS(ES) National Aeronautics and Space Administration Washington, DC 20546-0001		10. SPONSORING/MONITORING AGENCY REPORT NUMBER  NASA TM-4398		
11. SUPPLEMENTARY NOTES  Also prepared as AIAA-91-3248 (with color reproduction) for presentation at the AIAA 9th Applied Aerodynamics Conference, Baltimore, Maryland, September 23-25, 1991.				
12a. DISTRIBUTION/AVAILABILITY STATEMENT  Unclassified — Unlimited Subject Category 02		12b. DISTRIBUTION CODE		
13. ABSTRACT (Maximum 200 words)  Flow-field measurements on the leading-edge extension (LEX) of the F-18 High Alpha Research Vehicle (HARV) were obtained using a rotating rake with 16 hemispherical-tipped five-hole probes. Detailed pressure, velocity, and flow direction data were obtained through the LEX vortex core. Data were gathered during 1-g quasi-stabilized flight conditions at angles of attack ( $\alpha$ ) from 10° to 52° and at Reynolds numbers based on mean aerodynamic cord up to $16 \times 10^6$ . Normalized dynamic pressures and crossflow velocities clearly showed the primary vortex above the LEX and formation of a secondary vortex at higher angles of attack. The vortex was characterized by a ring of high dynamic pressure surrounding a region of low dynamic pressure at the vortex core center. The vortex core, subcore diameter, and vertical location of the core above the LEX increased with angle of attack. Minimum values for static pressure were obtained in the vortex subcore and decreased nearly linearly with increasing angle of attack until vortex breakdown. Rake-measured static pressures were consistent with previously documented surface pressures and showed good agreement with flow visualization flight test results. Comparison of the LEX vortex flight test data to computational solutions at $\alpha \approx 19^\circ$ and $30^\circ$ showed fair correlation.				
14. SUBJECT TERMS Computational fluid dynamics (CFD); F-18 airplane; Five-hole probes; High angle of attack; Vortex; Vortical flows			15. NUMBER OF PAGES 48	16. PRICE CODE A03
17. SECURITY CLASSIFICATION OF REPORT Unclassified	18. SECURITY CLASSIFICATION OF THIS PAGE Unclassified	19. SECURITY CLASSIFICATION OF ABSTRACT	20. LIMITATION OF ABSTRACT	